

DTIC FILE COPY

4

TECHNICAL REPORT BRL-TR-3076

AD-A218 749

BRL

DTIC FILE COPY

COMPARISON OF NAVIER-STOKES COMPUTATION AND
EXPERIMENT FOR POINTED, SPHERICAL, AND
FLAT TIPPED SHELL AT MACH 2.95

BERNARD J. GUIDOS
PAUL WEINACHT
DAVID S. DOLLING

JANUARY 1990



APPROVED FOR PUBLIC RELEASE; DISTRIBUTION UNLIMITED.

U.S. ARMY LABORATORY COMMAND

BALLISTIC RESEARCH LABORATORY
ABERDEEN PROVING GROUND, MARYLAND

DESTRUCTION NOTICE

Destroy this report when it is no longer needed. DO NOT return it to the originator.

Additional copies of this report may be obtained from the National Technical Information Service, U.S. Department of Commerce, Springfield, VA 22161.

The findings of this report are not to be construed as an official Department of the Army position, unless so designated by other authorized documents.

The use of trade names or manufacturers' names in this report does not constitute indorsement of any commercial product.

REPORT DOCUMENTATION PAGE

1a. REPORT SECURITY CLASSIFICATION UNCLASSIFIED		1b. RESTRICTIVE MARKINGS	
2a. SECURITY CLASSIFICATION AUTHORITY		3. DISTRIBUTION/AVAILABILITY OF REPORT Approved for public release, distribution unlimited.	
2b. DECLASSIFICATION/DOWNGRADING SCHEDULE			
4. PERFORMING ORGANIZATION REPORT NUMBER(S) BRL-TR-3076		5. MONITORING ORGANIZATION REPORT NUMBER(S)	
6a. NAME OF PERFORMING ORGANIZATION U.S. Army Ballistic Research Laboratory	6b. OFFICE SYMBOL (if applicable) SLCBR-LF	7a. NAME OF MONITORING ORGANIZATION	
6c. ADDRESS (City, State, and ZIP Code) Aberdeen Proving Ground, Maryland 21005-5066		7b. ADDRESS (City, State, and ZIP Code)	
8a. NAME OF FUNDING/SPONSORING ORGANIZATION	8b. OFFICE SYMBOL (if applicable)	9. PROCUREMENT INSTRUMENT IDENTIFICATION NUMBER	
8c. ADDRESS (City, State, and ZIP Code)		10. SOURCE OF FUNDING NUMBERS	
		PROGRAM ELEMENT NO. 62618A	PROJECT NO. 1L162618AH80
		TASK NO. 00	WORK UNIT ACCESSION NO. 001 AJ
11. TITLE (Include Security Classification) COMPARISON OF NAVIER-STOKES COMPUTATION AND EXPERIMENT FOR POINTED, SPHERICAL, AND FLAT TIPPED SHELL AT MACH 2.95			
12. PERSONAL AUTHOR(S) GUIDOS, BERNARD J., WEINACHT, PAUL, and DOLLING*, DAVID S.			
13a. TYPE OF REPORT Technical Report	13b. TIME COVERED FROM _____ TO _____	14. DATE OF REPORT (Year, Month, Day)	15. PAGE COUNT
16. SUPPLEMENTARY NOTES Department of Aerospace Engineering and Engineering Mechanics, The University of Texas at Austin, Austin, Texas 78712-1085			
17. COSATI CODES		18. SUBJECT TERMS (Continue on reverse if necessary and identify by block number)	
FIELD	GROUP	Computational Fluid Dynamics, Parabolized Navier-Stokes	
01	02	Unsteady Navier-Stokes, Supersonic Flow (Continued)	
01	04	Supersonic Wind Tunnel, Boundary Layer Transition	
19. ABSTRACT (Continue on reverse if necessary and identify by block number) A computational fluid dynamics study is described and results are shown for a tangent ogive-cylinder model with pointed, spherical, and flat nosetips at Mach number 2.95. The flow conditions simulate wind tunnel tests conducted at Princeton University Gas Dynamics Laboratory. The primary objective is to compare the computational and experimental results and assess the accuracy of the computational approach. Two thin-layer Navier-Stokes computational techniques are used in conjunction to compute the flow fields of interest. The first method computes the flow in the vicinity of the blunt nosetip and provides inflow conditions for the second method, which computes the flow over the remainder of the body, excluding the base region. An empirical boundary layer transition model is implemented to partially account for the experimentally observed transition. Comparisons are made of surface pressure, turbulent boundary layer velocity profiles, skin friction coefficient, and of the nosetip flow structure.			
20. DISTRIBUTION/AVAILABILITY OF ABSTRACT <input checked="" type="checkbox"/> UNCLASSIFIED/UNLIMITED <input type="checkbox"/> SAME AS RPT. <input type="checkbox"/> DTIC USERS		21. ABSTRACT SECURITY CLASSIFICATION UNCLASSIFIED	
22a. NAME OF RESPONSIBLE INDIVIDUAL Bernard J. Guidos		22b. TELEPHONE (Include Area Code) (301) 278-5436	22c. OFFICE SYMBOL SLCBR-LF-C

18. SUBJECT TERMS (Continued)

Blunt Body;
Velocity Profiles

Flow Separation
Skin Friction,

Table of Contents

	<u>Page</u>
List of Figures	v
List of Tables	vii
I. INTRODUCTION	1
II. WIND TUNNEL CONFIGURATIONS & FLOW CONDITIONS	1
III. COMPUTATIONAL APPROACH	2
1. THIN-LAYER UNSTEADY NAVIER-STOKES	3
2. THIN-LAYER PARABOLIZED NAVIER-STOKES	4
IV. COMPUTATIONAL ASPECTS OF THE PROBLEM	5
1. CODE COUPLING	5
2. NUMERICAL GRIDS	5
3. COMPUTER RESOURCES	6
V. BOUNDARY LAYER TRANSITION MODEL	7
VI. COMPARISON WITH EXPERIMENT	8
1. NOSETIP FLOW STRUCTURE	8
2. SURFACE PRESSURE	11
3. LONGITUDINAL VELOCITY PROFILES	12
4. SKIN FRICTION	13
VII. SUMMARY	16
Acknowledgments	17
References	41
List of Symbols	45
Distribution List	47

Accession For	
NTIS GRA&I	<input checked="" type="checkbox"/>
DTIC TAB	<input checked="" type="checkbox"/>
Unannounced	<input type="checkbox"/>
Justification	
By _____	
Distribution/ _____	
Availability Codes	
Dist	Full and/or Special
A-1	



INTENTIONALLY LEFT BLANK.

List of Figures

<u>Figure</u>		<u>Page</u>
1	Wind tunnel model and nosetip configurations	19
2	Physical and computational grid coordinates	20
3	Illustration of code coupling near blunt nosetip	21
4	Computational grid for nosetip R3, $\alpha = 0^\circ$	22
5	Computational grid for nosetip F3, $\alpha = 0^\circ$	23
6	Computed longitudinal skin friction coefficient showing effect of transition model, tip R3, $\alpha = 0^\circ$	24
7	Computed shocks and Mach contours (0.1-2.3 at 0.1 increments) and comparison with measured shocks, tip R3, $\alpha = 0^\circ$	25
8	Wind tunnel shadowgraph of flow over nosetip F3, $\alpha = 2.9^\circ$	26
9	Computed shocks and Mach contours (0.1-2.4 at 0.1 increments) and comparison with measured shocks, tip F3, $\alpha = 0^\circ$	27
10	Computed shocks and Mach contours (0.1-2.4 at 0.1 increments) and comparison with measured shocks, tip F3, $\alpha = 2.9^\circ$, wind side	28
11	Computed shocks and Mach contours (0.1-2.4 at 0.1 increments) and comparison with measured shocks, tip F3, $\alpha = 2.9^\circ$, lee side	29
12	Computed velocity vectors showing flow separation, tip F3, $\alpha = 0^\circ$	30
13	Computed particle paths showing flow separation, tip F3, $\alpha = 0^\circ$	31
14	Surface pressure comparison, tip R3, $\alpha = 0^\circ$	32
15	Surface pressure comparison, tip R3, $\alpha = 2.9^\circ$, wind and lee sides	33
16	Surface pressure comparison, tip F3, $\alpha = 0^\circ$	34
17	Surface pressure comparison, tip F3, $\alpha = 2.9^\circ$, wind side	35
18	Surface pressure comparison, tip F3, $\alpha = 2.9^\circ$, lee side	36
19	Velocity profile comparisons, tips P and R3, $\alpha = 2.9^\circ$, wind side	37
20	Velocity profile comparisons, tips P and R3, $\alpha = 2.9^\circ$, lee side	38
21	Velocity profile comparisons, tips P and F3, $\alpha = 2.9^\circ$, wind side	39
22	Velocity profile comparisons, tips P and F3, $\alpha = 2.9^\circ$, lee side	40

INTENTIONALLY LEFT BLANK.

List of Tables

<u>Table</u>		<u>Page</u>
1	Computational Resources	7
2	Comparison of Bow Shock Detachment Distance (cal) at Model Axis, $\alpha = 0^\circ$	10
3	Comparison of Bow Shock Radius of Curvature (cal) at Model Axis, $\alpha = 0^\circ$	11
4	Comparison of Skin Friction Coefficient ($C_f \times 10^3$)	15

INTENTIONALLY LEFT BLANK.

I. INTRODUCTION

Interest in predicting nosetip bluntness effects on projectile aerodynamics at the US Army Ballistic Research Laboratory (BRL) stems from the fact that almost all Army projectiles are blunt. Designers recognize the fact that nosetip bluntness alters the total drag of shell.¹ Computational and experimental research has shown that nosetip bluntness alters the Magnus characteristics of spinning shell.^{2,3} The effects are manifested through detailed flow elements like the three-dimensional boundary layer and bow shock entropy wake. An accurate predictive capability will give designers a new tool for determining when the aerodynamic effects are important. With the computational power of the current generation of supercomputers, the flow can be simulated through large scale Navier-Stokes computations.

The importance of validating blunt body simulations with experimental measurements was affirmed in Reference 2. Predictions of the Magnus effect for models with pointed, spherical, and flat nosetips were compared to wind tunnel measurements at Mach 3. The comparisons between computation and experiment for the sharp and spherical nosetip models were good, while the comparison for the flat nosetip model was poor. The findings were attributed to (1) the higher complexity of the flow over the flat nosetip compared to the spherical nosetip and (2) the lack of sufficient size and speed of available computational resources to accurately model the flow over the flat nosetip.

A new experimental study was conducted to measure the effects of bluntness on the flow over a body of revolution and to provide a set of data for computational fluid dynamics (CFD) code validation. Wind tunnel tests^{4,5,6,7} were done at Princeton University Gas Dynamics Laboratory for a tangent ogive-cylinder model with several different nosetips. Surface pressure measurements and boundary layer pitot pressure surveys were made, and shadowgraphs were obtained at a free-stream Mach number of 2.95. The tests provide details of the flow with enough accuracy to be considered baseline data for assessing computational predictions.

A computational study was undertaken at the BRL using thin-layer Navier-Stokes techniques to simulate the Princeton tests. Supercomputer resources not available for the study of Reference 2 were used. The objective was to compare the computational results with the wind tunnel measurements and assess the accuracy of the CFD approach. The results of the study are presented herein. Details concerning the application of the numerical techniques are documented to serve as a benchmark for future applications.

II. WIND TUNNEL CONFIGURATIONS & FLOW CONDITIONS

The computations simulate wind tunnel tests conducted at the Princeton University Gas Dynamics Laboratory 20 cm by 20 cm Mach 3, high Reynolds number, blowdown tunnel.^{4,5,6,7} The models, instrumentation, techniques, and data acquisition and reduction are discussed in detail in the listed references. A brief description is given here to provide

a background for the ensuing discussions

The wind tunnel model and nosetip configurations are shown in Figure 1. The pointed model consists of a 3 caliber (cal) tangent ogive nose and a 5 cal cylindrical section. The reference diameter (i.e. that of the cylinder) is 4.95 cm (1.95 inches).

Six blunted nosetips were manufactured to screw into the basic configuration in place of the pointed nosetip. Each blunt nosetip was machined as a truncation of the pointed nosetip. Designations for each nosetip are taken directly from the reference documentation. The pointed nosetip is designated P; the spherical nosetips are designated R1, R2, and R3; the flat nosetips are designated F1, F2, and F3.

The bluntness ratios, defined as the ratio of fuze tip diameter to reference diameter, were 5%, 12.5%, and 25%. In the case of a spherical nosetip, the fuze tip diameter is defined as twice the radial distance from the axis to the juncture of the sphere and ogive. For a flat nosetip, the fuze tip diameter is defined as twice the radial distance from the axis to the juncture of the flat face and ogive.

The model was supported at the base by an axial sting and held fixed relative to the free stream. Wall pressure distributions, pitot pressure surveys, and shadowgraphs were obtained. Longitudinal (streamwise) velocity profiles were generated from the pitot surveys which were taken at three axial locations on the cylinder. The shadowgraphs provided a means for locating the bow shock, the boundary layer transition zone, and, in the case of a flat nosetip, the imbedded recompression shock.

Conditions for the computations are taken as the average over numerous wind tunnel runs. The Mach number is 2.95, with angles of attack of 0° and 2.9° . The nominal stagnation temperature is 260K, the nominal Reynolds number is 3.14×10^6 based on model diameter, and the stagnation pressure is 6.89×10^5 N/m (6.8 atm). The wall temperature is taken as adiabatic and the flow is assumed to be steady. Boundary layer transition occurred in the experiment without the use of a tripping device, and varied widely between the different nosetips. The computational simulation of transition is discussed in a separate section.

Nosetips P, R3, and F3 provide the best data with which to make detailed flow comparisons. Nosetip P provides the reference case for discerning the effects of bluntness. Nosetips R3 and F3 most clearly illustrate the effects due to their comparatively large scales, and are therefore the primary focus of this report.

III. COMPUTATIONAL APPROACH

The computational methodology consists of two separate techniques applied in succession. An unsteady Navier-Stokes (UNS) technique is used to compute the flow in the vicinity of each blunt nosetip. These solutions provide initial conditions for a parabolized Navier-Stokes (PNS) technique, which computes the flow by integrating, or marching, in the streamwise direction. The use of these two techniques is an efficient way to model the flow because the unsteady (time-iterative) technique, which is considerably more compu-

tationally intensive, is applied over a relatively small region near the blunt nosetip. The parabolized (space-marching) technique, which processes only two physical planes of data simultaneously, is applied over the remaining downstream region, excluding the base.

1. THIN-LAYER UNSTEADY NAVIER-STOKES

Computational modeling of the flow over the blunted nosetips was accomplished using the thin-layer UNS approach first reported by Pulliam and Steger.⁸ This technique integrates the transformed, time-dependent, thin-layer, Navier-Stokes equations in strong conservation law form, given as:

$$\frac{\partial \hat{q}}{\partial \tau} + \frac{\partial \hat{E}}{\partial \xi} + \frac{\partial \hat{F}}{\partial \eta} + \frac{\partial \hat{G}}{\partial \zeta} = \frac{1}{\hat{R}e} \frac{\partial \hat{S}}{\partial \zeta} \quad (1)$$

Equation (1) represents conservation of mass, momentum, and energy in the transformed coordinate directions for large Reynolds number flow. The vector \hat{q} is the transformed vector of dependent variables. The vectors \hat{E} , \hat{F} , and \hat{G} are the transformed inviscid flux vectors. The vector \hat{S} is the vector of viscous terms that result from the thin-layer approximation for large Reynolds number flows. Ideal gas behavior is assumed.

The transformed coordinates, Figure 2, are :

$\tau = t$ is time

$\xi = \xi(t, x, y, z)$ is the longitudinal (streamwise) coordinate

$\eta = \eta(t, x, y, z)$ is the circumferential coordinate

$\zeta = \zeta(t, x, y, z)$ is the near-normal coordinate

The transposed vector of dependent variables,

$$\bar{q}^T = (\rho, \rho u, \rho v, \rho w, e),$$

is obtained at each grid point using the approximately factored, implicit, delta form, finite-difference algorithm of Beam and Warming.⁹ Second order central differencing is used in the three coordinate directions. Fourth order explicit and second order implicit smoothing terms are added to suppress high frequency oscillations in the solution. The solution at each time step requires a series of block-tridiagonal matrix inversions (sweeps) in each of the transformed coordinate directions. For the spherical tip cases at non-zero incidence, a directionally hybrid implicit/explicit algorithm¹⁰ was applied, eliminating implicit sweeps in the η and ξ directions in favor of explicit sweeps.

The outer boundary, which consists of the bow shock, is shock fitted using an explicit procedure.¹¹ At the body surface, the no-slip velocity boundary condition is enforced, and the pressure is updated explicitly from the normal momentum equation evaluated at the wall. The downstream (outflow) boundary employs a linear (constant outflow gradient) extrapolation along outflow grid lines. For the cases at non-zero incidence, bilateral symmetry conditions are imposed about the pitch plane. For the cases at zero incidence, i.e.

axisymmetric flow, only one circumferential grid plane is used. The flow field initialization procedure is described in detail in Reference 11.

These earlier studies have shown substantial accuracy in computing the flow over blunted reentry vehicles using this Beam/Warming central difference approach.¹⁰⁻¹²

2. THIN-LAYER PARABOLIZED NAVIER-STOKES

Computational modeling of the flow over the ogive and cylinder (and the pointed nosetip) was accomplished using the thin-layer PNS technique first reported by Schiff and Steger.¹³ This technique spatially integrates the transformed, steady, thin-layer Navier-Stokes equations in strong conservation law form, given as:

$$\frac{\partial \hat{E}_s}{\partial \xi} + \frac{\partial \hat{F}}{\partial \eta} + \frac{\partial \hat{G}}{\partial \zeta} = \frac{1}{\hat{R}e} \frac{\partial \hat{S}}{\partial \zeta} \quad (2)$$

Equation (2) represents the thin-layer approximation to steady-state conservation of mass, momentum, and energy in the three coordinate directions. \hat{E}_s , \hat{F} , and \hat{G} are the inviscid flux vectors. \hat{E}_s is a modified flux vector resulting from the subsonic sublayer approximation.¹³ The vector \hat{S} is the vector of viscous terms that result from the thin-layer approximation. Ideal gas behavior is assumed.

The transformed coordinates, Figure 2, are:

$\xi = \xi(x)$ is the axial (marching) coordinate

$\eta = \eta(x, y, z)$ is the circumferential coordinate

$\zeta = \zeta(x, y, z)$ is the radial coordinate

The vector of dependent variables,

$$\bar{q}^T = (\rho, \rho u, \rho v, \rho w, e),$$

is obtained at each grid point using the approximately factored, implicit, delta form, finite-difference algorithm of Beam and Warming.⁹ Second order central differencing is used in the circumferential and radial directions, and first order one-sided differencing is used in the marching direction. Fourth order explicit smoothing is added to suppress high frequency oscillations in the solution. The solution is advanced downstream by numerically integrating in the direction parallel to the projectile axis. Each spatial (marching) step requires a series of block tridiagonal matrix inversions (sweeps) in the circumferential and radial directions.

The outer boundary, which consists of the bow shock, is shock fitted using an implicit procedure.¹⁴ At the body surface, the no-slip condition is enforced and the pressure is obtained from the subsonic sublayer approximation, i.e the pressure across the subsonic portion of the viscous layer is held constant. Bilateral symmetry conditions are imposed at the pitch plane.

Initial conditions for the pointed nosetip configuration are generated using the PNS method in step-back mode.¹³⁻¹⁶ This application of the technique assumes conical flow conditions near the tip of the projectile and iteratively refines the solution to satisfy this assumption.

IV. COMPUTATIONAL ASPECTS OF THE PROBLEM

1. CODE COUPLING

The PNS procedure requires initial conditions for downstream marching. Initial conditions for marching consist of two adjacent ξ grid planes where the vector of dependent variables is known. For the blunt nosetip cases, the converged UNS solutions were utilized, as illustrated in Figure 3. Each nosetip solution was non-conservatively interpolated onto a PNS grid at two adjacent axial stations. The circumferential grid distribution was retained exactly, and the dependent flow variables were linearly interpolated in the radial direction.

The location of initial conditions for the PNS computations was selected far enough downstream to avoid large streamwise gradients and, in the case of the F3 nosetip, flow separation around the corner of the flat face. The initial data location was also taken far enough upstream from the UNS outflow boundary to avoid anomalies associated with the constant gradient outflow condition. Trial and error in the early stages of the study revealed solution inaccuracies in either extreme. By properly selecting the UNS outflow boundary and PNS initial data plane, coupling was achieved using the PNS code with nominal values of smoothing for bodies of revolution in this flow regime at small incidence.¹⁶

2. NUMERICAL GRIDS

All computational grids of this study were generated algebraically. As usual for viscous flow computations, grid points were exponentially clustered near the body to ensure adequate resolution of the boundary layer. The grid dimensions for the UNS solutions are shown in Table 1. For the axisymmetric flow cases, a single circumferential plane was used. For the angle of attack cases, where bilateral symmetry exists, 21 circumferential planes were distributed from $\phi = -10^\circ$ to $\phi = 190^\circ$ at 10° increments.

Figure 4 shows the computational grid for nosetip R3 (converged solution, $\alpha = 0^\circ$). The free-stream flow is left to right, and the outer boundary represents the converged, fitted bow shock. The x coordinate is measured from the virtual origin, defined as the intersection of a fully extended ogive and the model axis. The spherical nosetip grids were generated from an existing wrap-around, spherical grid¹¹ approach which was modified² by appending an ogive nose section tangent to the spherical tip. The ogive extension, with lines of constant $\xi - \eta$ becoming radially oriented downstream of the nosetip, facilitates coupling with the PNS code. As the results will indicate, the large streamwise pressure gradient that exists at the nosetip region is substantially reduced on the ogive section.

Figure 5 shows the computational grid for nosetip F3 (converged solution, $\alpha = 0^\circ$).

This wrap-around grid consists of straight line segments between the body and shock. At the corner of the flat face, the constant $\xi - \eta$ line intersects the body at a 45° angle with respect to the projectile axis. The flat nosetip geometry is arrived at during the flow field solution procedure by truncating a small portion of the (initially) spherical nosetip, regenerating the grid and bow shock, and allowing the solution to relax completely (about 500 time steps). This is done several times until the final body shape is obtained, and inherently requires a larger number of time steps to obtain the final solution compared to the spherical nosetip computations. The current grid is a result of further modifications to the approach of Reference 2 in that the orientation of constant $\xi - \eta$ lines varies more slowly near the corner. This modification was found to be vital for retaining accuracy and stability of the numerical scheme for this problem.

The PNS computations were performed using cylindrical grids. In the radial direction, 45 grid points were used with exponential clustering near the body. For solutions having bilateral symmetry, circumferential planes were distributed from $\phi = 0^\circ$ to $\phi = 180^\circ$ at 10° increments. Some additional cases were run using 5° increments, but the flow properties of interest remained unaffected. For axisymmetric solutions, only three circumferential planes were used at $\phi = 0^\circ$, $\phi = 90^\circ$, and $\phi = 180^\circ$ in order to employ a tested¹⁶ cylindrical coordinate formulation¹⁴ of the PNS equations. The grid density in the marching direction varied from 300 to 500 marching steps over a length of approximately 8 cal.

3. COMPUTER RESOURCES

A major advantage of this study compared to the study of Reference 2 was the availability of Cray X-MP and Cray 2 computers. These resources were especially valuable in the case of the F3 nosetip, where accuracy, not computational efficiency, was the main consideration in light of the dubious results of Reference 2. A substantial increase in grid resolution was implemented in order to capture the streamwise flow separation which was expected to occur around the corner of the flat face. Techniques for reducing the computing time were not investigated. These could have included the optimization of the time step increment and grid distribution, the maximum utilization of the vector processing and expanded memory, the application of the implicit/explicit hybrid scheme, and the use of a CFT77, rather than a CFT, Fortran compiler.

In the context of the above considerations, the UNS computing times are listed in Table 1. The CPU times in Table 1 represent solutions that satisfy certain convergence criteria. For the spherical nosetips, these criteria are: (a) the maximum Courant number, initially about 5, is eventually raised to about 50-80; (b) the maximum dimensionless shock speed relative to the body is less than 0.01; and (c) the L_2 residual for the i th time step is less than 10^{-7} . The L_2 residual is defined as

$$L_2^i = \frac{1}{\Delta t + .0005} \sqrt{\frac{1}{m_{total}} \sum_{n=1}^5 \sum_{m=1}^{m_{total}} (q_n^i - q_n^{i-1})^2} \quad (3)$$

where Δt is the time increment for the i th integration step, q_n^i is the n th element of the dependent variable vector \bar{q} at the i th integration step, m is an individual grid point, and m_{total} is the total number of grid points. For the flat nosetips, these criteria are:

(a) the maximum Courant number is about 10; (b) and (c) as given above; and (d) the velocities in the separated region (which proved to be the most locally sensitive indicator of convergence), became virtually steady.

The PNS computing times are based on marching the starting plane data a distance of 8 cal downstream. For the axisymmetric cases, the CPU time was about 2 minutes on a CDC 7600 or 30 seconds on a Cray X-MP. For the non-axisymmetric cases, the CPU time was about 15 minutes on a CDC 7600 or 3 minutes on a Cray X-MP.

Table 1. Computational Resources

Nosetip & Incidence	MESH SIZE long-norm-circ	COMPUTER	MEMORY (Mwords)	CPU TIME	NUMBER OF ITERATIONS
R1 $\alpha = 0^\circ$	30x30x1	Cray X-MP	0.13	8 min	2500
R2 $\alpha = 0^\circ$	40x30x1	Cray X-MP	0.14	9 min	2500
R3 $\alpha = 0^\circ$	50x30x1	Cray X-MP	0.15	10 min	2500
F3 $\alpha = 0^\circ$	119x60x1	Cray 2	0.30	7.0 hrs	18000
R1 $\alpha = 2.9^\circ$	30x30x21	Cray X-MP	0.44	1 hrs	2500
R2 $\alpha = 2.9^\circ$	40x30x21	Cray X-MP	0.50	1.5 hrs	2500
R3 $\alpha = 2.9^\circ$	50x30x21	Cray X-MP	0.55	3 hrs	3000
F3 $\alpha = 2.9^\circ$	119x60x21	Cray 2	2.50	40 hrs	5000

V. BOUNDARY LAYER TRANSITION MODEL

The pitot surveys in the experiment were taken at three different axial locations on the cylinder, where the flow was turbulent. Boundary layer transition can be seen in the shadowgraphs to vary as a function of nosetip geometry, angle of attack, and roll angle. Overall, transition began approximately 0.5-2.5 cal from the virtual origin and extended approximately 0.25-0.5 cal downstream. The sensitivity of the numerical results to location and length of transition was investigated using the shadowgraphs as a guide. Laminar flow conditions were used in all of the UNS computations. Transition was simulated in the PNS computations in the following manner:

The effective viscosity, usually defined as

$$\mu = \mu_l + \mu_t \quad (4)$$

is re-defined as

$$\mu = \mu_l + \kappa_t \mu_t \quad (5)$$

where μ_l is the laminar (molecular) viscosity, μ_t is the turbulent viscosity obtained from the Baldwin-Lomax model,¹⁷ and κ_t is the transition intermittency factor. This factor is identically zero for laminar flow and identically one for fully turbulent flow.

From probability considerations for a turbulence spot production function, Dhawan and Narasimha¹⁸ derived a distribution of transition intermittency that agreed with a

survey of wind tunnel measurements over a flat plate. The distribution took the form

$$\kappa_t = 1 - \exp(-A(x - x_t)^2) \quad \text{for } x > x_t \quad (6)$$

where A is a positive constant that represents the rate of transition and x_t is the location where transition begins. The the location and length of transition are not prescribed a priori, but are instead empirically based. A similar distribution which is more easily applied to parametric study is the polynomial

$$\kappa_t = 10\left[\frac{x - x_1}{x_2 - x_1}\right]^3 - 15\left[\frac{x - x_1}{x_2 - x_1}\right]^4 + 6\left[\frac{x - x_1}{x_2 - x_1}\right]^5 \quad \text{for } x_1 < x < x_2 \quad (7)$$

where x_1 and x_2 mark the beginning and end of transition. The properties of this polynomial are (1) it varies from zero to one in the domain of interest, (2) it has zero slope at the endpoints, and (3) it is symmetric about the midpoint. Equation (7) was used in the PNS computations to simulate transition. Effects due to surface curvature, pressure gradient, or nosetip geometry itself, are not accounted for in the model. Variations with respect to roll angle due to model incidence are also ignored.

Several computations were performed in which the location and length of transition were varied to determine the sensitivity of the downstream solution. The length of the transition region was maintained large enough to avoid creating numerical pressure oscillations at the surface, yet small enough to achieve fully turbulent flow upstream of the ogive-cylinder juncture, as depicted in the shadowgraphs.

Figure 6 shows the computed skin friction coefficient C_f as a function of axial position for three different transition locations and lengths, using Equation (7). In the transition region, the skin friction is quite different as expected and resembles the variations shown in Reference 18. In the region just downstream of transition, the skin friction for each case is nearly identical. Then a history effect becomes evident, with C_f varying by about 10% at $x/d=8$. The effect on the surface pressure and the turbulent velocity profiles at the survey stations was negligible. With this degree of sensitivity in hand, the ensuing PNS computations were performed by specifying transition to begin at the initial data plane and extend approximately one caliber downstream.

VI. COMPARISON WITH EXPERIMENT

1. NOSETIP FLOW STRUCTURE

The supersonic flow over a flat nosetip is clearly more complex than the flow over a spherical nosetip.^{19,20} The geometric discontinuity associated with the flat nosetip shoulder causes sharp flow gradients and over-expansion. If the shoulder radius is small enough, the flow separates and the recompression occurs through an oblique shock.

One set of measurements, at $M=2$, have shown the flow to overexpand and recompress even for a spherical nosetip.²¹ Therefore, the possibility of the recompression waves coalescing into an oblique shock in the absence of flow separation, in general, should not be ruled out. The shadowgraphs of this study, however, clearly show that recompression shocks formed for the flat nosetips only.

Figure 7 shows the computed Mach contours for nosetip R3, $\alpha = 0^\circ$, along with the computed and measured bow shock locations. The computed bow shock location agrees with experiment to within the accuracy of the measurement (which is discussed subsequently). The computed Mach contours illustrate the smooth expansion that occurs around the nosetip for this case. Such smoothness in the flow field is a computational asset because, compared to a flat nosetip, less grid resolution is required.

Figure 8 is a reproduction of the wind tunnel shadowgraph of nosetip F3, $\alpha = 2.9^\circ$. The shadowgraphs were taken to provide qualitative information on the flow structure. The bow and recompression shocks are visible and their locations were measured to compare with the computations. The recompression shock, in particular, appears to be a sensitive indicator of computational accuracy.

The bow and recompression shock locations were measured using transparencies of the shadowgraphs overlaid onto a fine Cartesian mesh. Severe optical distortion from the large density gradients at the nosetip prohibited direct measurement relative to the vertex of the actual nosetip. Reference marks were not made on the tunnel window or on the model itself, compounding the difficulty in obtaining quantitative data. Instead, the apparent bow shock vertex was used as the reference point for the readings. The uncertainty in the measured distance between any two points in the shadowgraphs was found to be approximately ± 0.002 calcs.

To locate the actual position of each nosetip, approximately twenty data points were taken along the ogive and fitted to the equation of the ogive using least squares. The intersection of the fitted curve and the body axis was taken as the virtual origin. The distance from this point to the actual blunt nosetip was then taken to be the value given for each configuration in Reference 5. The uncertainty in the absolute radial location of the measured points was found to be approximately ± 0.002 calcs. The uncertainty in the absolute axial location of the measured points varied between nosetips, and is given in Table 2.

The measured shock patterns are plotted as points in Figures 9-11, which show the computed Mach contours for nosetip F3, $\alpha = 0^\circ$ and $\alpha = 2.9^\circ$. The strong expansion at the corner is visible in the computations, but the recompression shock is less obvious. The computed imbedded shocks are instead visualized in the plot as thickened solid lines. These lines represent surfaces where the velocity component in the direction of the pressure gradient is equal to the local sound speed, and the Mach number in that direction is decreasing.²² The shock relations are not presumed to be satisfied, as evidenced by the presence of the small, disconnected patches near the body.

The comparison of the computed and measured shock patterns in Figures 9-11 is approximately within the accuracy of the measurement in each case. Because of the limits in measurement accuracy previously discussed, the positions of the bow and recompression shocks relative to each other may be more indicative of agreement than the absolute comparisons. The trends with respect to incidence are well-predicted along the pitch-plane, with the bow shock moving closer to the body on the wind side and farther from the body on the lee side. The recompression shock can be clearly seen to move upstream on the wind side and downstream on the lee side. In Figures 9 and 10, the slight bend in

the recompression shock is apparent in both computation and experiment. The comparisons lend credence to the previously mentioned method of locating imbedded shocks in a computational flow field solution.

A more quantitative comparison of bow shock detachment distance is shown in Table 2. The approximate measurements made in Reference 5 are shown in addition to the measured values obtained independently during this study. The computed standoff distances compare with the measured values which were obtained using the above procedure to approximately within the measurement accuracy. Other values of shock detachment distance at $M=2.95$ are shown from both analytical and experimental sources, but with different free-stream conditions.²²⁻²⁵

Table 2. Comparison of Bow Shock Detachment Distance (cal) at Model Axis, $\alpha = 0^\circ$

	Nosetip			
	R1	R2	R3	F3
UNS Comp.	.0059	.0145	.0290	.0813
Experiment	N/A	.011±.0025	.0275±.0025	.084±.006
Exp - Ref 5	N/A	N/A	N/A	.079
Reference 23	.0049	.0123	.0246	.0824
Reference 24	.0051	.0121	.0248	.0717
Reference 25	.0042	.0111	.0218	N/A
Reference 26	.0073	.0160	.0313	N/A

Following Reference 5, an additional comparison of bow shock shape was made by obtaining the bow shock radius of curvature on the model axis. A series of least squares fits was made of the generalized conic equation

$$r_s^2 = 2Rx_s - Bx_s^2 \quad (8)$$

where r_s is the radial distance from the axis to the shock, x_s is the axial distance from the shock vertex, R is the shock radius of curvature on the axis, and B is the shock bluntness parameter, which characterizes the eccentricity. Van Dyke²⁷ used Equation (8) to characterize bow shock shapes in a pioneering numerical approach.

The computed and measured bow shock radius of curvature on the axis for each nosetip at $\alpha = 0^\circ$ is shown in Table 3. The values from Reference 5 are shown in addition to the experimental values obtained from the fits made independently in this study. Additional values are included from a compilation²⁸ of range and wind tunnel data for spheres and spherically blunted shell. The comparison of the computations with the values from Reference 5 shows poor agreement. The comparison with the values from Reference 28 and the values obtained independently during this study, however, is within 7.5%.

Bow shock shape parameters of spheres and spherical nosetips are commonly normalized by the sphere radius. If the viscous effects are small, the normalized parameters should be nearly constant for all three spherical nosetips in this study. In Table 3, such normalization yields a non-dimensional R of 1.51 ± 0.05 for the computations and Reference

28. The non-dimensional R for Reference 5, however, varies significantly for each of the spherical nosetips, indicating that those values are not consistent with each other. The reason for this discrepancy is not clear, but the values generated independently in this study fare better in this test of consistency.

Table 3. Comparison of Bow Shock Radius of Curvature (cal) at Model Axis, $\alpha = 0^\circ$

	Nosetip			
	R1	R2	R3	F3
UNS Computation	.038	.098	.198	.343
Experiment	.041	.101	.213	.366
Exp - Ref 5	.042	.084	.165	.243
Reference 28	.040	.102	.202	N/A

A comparison of shock bluntness parameter B is not included here for several reasons. The bluntness parameter is more indicative of the shock shape further downstream rather than close to the nosetip. The sensitivity of B to fits of Equation (8) was found to be quite large. In fact, Equation (8) may only be valid near the stagnation region since it implicitly assumes that the shock is generated by a body which is a conic surface. The configurations of interest in this study are more aptly described as piecewise conic.

Whether flow separation occurs around the shoulder of the flat nosetip is difficult, if not impossible, to determine from the shadowgraphs. Figures 12 and 13 show close up views of the computed velocity vectors and particle traces for nosetip F3, $\alpha = 0^\circ$. The computation shows that the flow separates at the corner and reattaches approximately one tenth of a cal downstream. The particle traces show a secondary separation region within the main region. Figures 12 and 13 illustrate the need for a high density grid near the corner to adequately resolve the separation region. This was a computational aspect which was not achieved in the study of Reference 2, where separation was not captured in the numerical solution of flow over a flat nosetip.

2. SURFACE PRESSURE

The accuracy of the surface pressure measurements is reported in Reference 6 to be typically $\pm 1.0\%$ of the free stream static pressure. Larger variations in the data, due to changing stagnation conditions over the duration of the experiments, are indicated by the tables of Reference 6. For nosetip F3, $\alpha = 0^\circ$, the stagnation point pressure varies in different runs from $p/p_\infty = 11.38$ to $p/p_\infty = 11.72$, about $\pm 3\%$. Downstream, different transducers were used, and the largest variation indicated from the tables also occurs for nosetip F3, $\alpha = 0^\circ$. At the sixth pressure tap, at $x/d \approx 0.48$, the measured value of pressure varies in different runs from $p/p_\infty = 1.452$ to $p/p_\infty = 1.603$, about $\pm 5\%$. These two examples are important indicators of experimental accuracy in the sense that nominal free-stream conditions were used in the computations.

Figures 14 and 15 show the comparison of the computed and measured surface pressure

for nosetip R3, $\alpha = 0^\circ$ and $\alpha = 2.9^\circ$. A smooth variation of pressure along the body is indicated. The flow does not overexpand. The agreement between computation and experiment is within the experimental accuracy, and the influence of small angle of attack is consistent. At $\alpha = 2.9^\circ$, some minor waivering of the computed pressure near the nosetip vertex is shown, a slowly damping numerical oscillation.

Figures 16-18 show the comparison of the computed and measured surface pressure for nosetip F3, $\alpha = 0^\circ$ and $\alpha = 2.9^\circ$. Near the stagnation point, the pressure agrees to within the experimental accuracy. The third pressure tap, located on the flat face of the nosetip, shows that the locally subsonic flow is already expanding before it reaches the corner. Whereas the computation shows a moderate disagreement with the measurement at this tap location, the severe expansion appears to be qualitatively captured in the numerical solution. A closer examination of the grid (Figure 5) and the Mach contours (Figures 9-11) reveals that much of this expansion is captured near the body surface between two adjacent grid points, indicating that agreement might be improved by adding, or clustering, grid points even closer to the corner. The tail end of the computed expansion shows a slight overshoot before recovering to a pressure level more comparable to that of the first tap downstream of the corner.

Downstream of the corner, the flow overexpands and recompresses in both the computation and the experiment. The computed pressures in the overexpanded region compare with the fifth pressure tap to within the measurement accuracy for $\alpha = 0^\circ$ and $\alpha = 2.9^\circ$, wind side. For $\alpha = 2.9^\circ$, lee side, the measured pressure is slightly lower than the computed pressure. The locations of the recompression correspond well for $\alpha = 0^\circ$ and $\alpha = 2.9^\circ$, wind side. For $\alpha = 2.9^\circ$, lee side, the computed recompression at the surface may occur slightly farther downstream than in the experiment. These observations are consistent with Figures 9-11 where the recompression location corresponds to the imbedded shock location. In all three cases, however, the computed surface pressure recovery levels agree with the experiment to within the measurement accuracy.

The pressure distribution and flow structure at the nosetip are important indicators of the localized effects of bluntness. Farther downstream, as reported in References 5-7, the surface pressure shows a variation of only $\pm 1.5\%$ between the seven different nosetips. A more sensitive indicator of bluntness must be utilized for purposes of computational validation, i.e the velocity profiles.

3. LONGITUDINAL VELOCITY PROFILES

Accurate prediction of the boundary layer velocity profiles is vital for determining the Magnus characteristics of a projectile. The Magnus force depends upon the interaction of cross flow and surface spin, even though it is predominantly a pressure, rather than a shearing, force.¹⁶ The most obvious effect of nose bluntness on the velocity profiles is a velocity deficit, and the bow shock entropy wake is usually considered to be the main contributor. However, it is interesting to note that a preliminary computation of the flat nosetip which failed to resolve the separation at the corner also failed to predict the velocity deficit in the downstream profile. This provided an indication that an accurate prediction of the separated corner flow is vital for predicting the downstream flow.

The comparisons of computed and measured velocity profiles presented here inherently contain uncertainties. For the measured profiles, these include effects of instrument calibration shifts, model misalignment, probe bending, assumptions used for reducing pitot pressure surveys to velocity profiles (for example, that of constant static pressure across the boundary layer), and variations in stagnation conditions both during and between runs. For the computed profiles, the most notable effect is probably turbulence modeling (see, for example, Reference 29). As discussed in an earlier section, transition had a minimal effect on the profiles in the fully turbulent region. In the comparisons presented here, nosetip P is included as a reference for discerning the effects of bluntness on the profiles. A comparison of the blunt nosetip profiles relative to the pointed nosetip profiles is an important consideration in determining how well the bluntness effects are being modeled computationally.

Figures 19 and 20 show the velocity profile comparisons for nosetips P and R3, $\alpha = 2.9^\circ$. Throughout most of the boundary layer, the absolute agreement between computation and experiment is within 5%. The exception is at the second station on the lee side, where the agreement is within only about 8-9%. In all cases, however, the comparison worsens within about 0.05 cm from the wall, but with no clear trend. The comparisons of the R3 profiles relative to the P profiles show favorable agreement. There is close agreement with the recovery that the R3 profile exhibits over the three axial stations. On the wind side, Figure 19, both computation and experiment show the velocity deficit of the R3 profile relative to the P profile to be minimal. On the lee side, Figure 20, both show the boundary layer edge of the spherical nosetip profiles to extend outward beyond the edge of the pointed nosetip profiles. There is also agreement in the outward migration of the merging of the profiles as x/d increases. The slight bulge in the the measured wind side profiles at $x/d=6.33$, 0.05 cm from the wall, occurred for all nosetips and may be an interference effect.

Figures 21 and 22 show the velocity profile comparisons for nosetips P and F3, $\alpha = 2.9^\circ$. Throughout most of the boundary layer, the absolute agreement between computation and experiment is within about 3%. The exception, again, is at the second station on the lee side, nosetip P, where the agreement worsens. And again, in all cases, the comparison worsens within 0.05 cm from the wall, but with no clear trend. Similar to the R3 profiles, the comparisons of the F3 profiles relative to the P profiles show favorable agreement. Both computation and experiment show the velocity deficit for the flat nosetip to be greater than for the spherical nosetip. On the wind side, Figure 21, there is favorable agreement with the velocity deficit in the F3 profiles, in the recovery of the F3 profiles relative to the P profiles over the three axial stations, and in the inward migration of the radial location where the profiles merge. On the lee side, Figure 22, the effects of blunting are seen to be most drastic. Both computation and experiment show the lack of recovery of the F3 profile relative to the P profile.

4. SKIN FRICTION

The experimental values of skin friction were generated in Reference 5 using a boundary-layer analysis code originally developed by Sun and Childs.³⁰ It uses an iterative technique

to fit the data to the combined law of the wall / law of the wake. The wall/wake parameters are varied until the deviation of the data from the combined law is minimized. The accuracy of C_f is estimated to be better than $\pm 10\%$. It should be noted that skin friction was presented in References 5,6, and 7 and was normalized using edge conditions as reference values for density and velocity. Here, C_f has been rescaled using undisturbed free-stream reference values of density and velocity. Thus, ambiguities associated with the determination of the boundary layer edge are removed from the comparison. The rescaled values of C_f are presented for all nosetips in order to provide a complete set of data for future reference.

The computational values of skin friction coefficient were obtained using a first order approximation of the derivative of the longitudinal velocity with respect to the radial coordinate at the wall. The first computational grid point from the wall was held to $3 \leq y^+ \leq 5$ units from the body through the use of an existing adaptive grid approach.¹⁶ In this range, the grid point location can easily affect the computed value of skin friction by $\pm 5\%$. The effect of the transition model on the computed C_f was already shown in a previous section to be at least $\pm 5\%$ at the third survey station but to be minimal at the first survey station. The effect of the wall temperature condition on the computed C_f was investigated and found to be detectable but minimal. A test case was computed where the wall temperature condition was prescribed as $T_w/T_r=1.03$ instead of adiabatic.⁶ The computed C_f for the test case was approximately 3% less at all locations downstream of the transition region. These sources of uncertainty in the computed skin friction combined give an estimated precision of at least $\pm 10\%$.

Table 4 shows the computationally and experimentally derived skin friction coefficients. The measured trend of decreasing skin friction with increased nose bluntness is well-predicted in the computation. Both computation and measurement show that, compared to the P nosetip, C_f is affected by the R1 nosetip by no more than 5%. Both show C_f is affected by the R2 nosetip by 5-15%; R3 by 10-20%; F3 by 15-25%.

For $\alpha = 0^\circ$, the absolute agreement of C_f is within 6% for all nosetips at each of the three measurement stations on the cylinder. The computed values of skin friction appear to straddle the measured values with no clear trend of over-prediction or under-prediction.

For $\alpha = 2.9^\circ$, wind side, the absolute agreement between computation and experiment decreases with increasing x/d , varying from 2% to 15%. Further downstream, the computation underpredicts the measured values of skin friction for all nosetips. This trend is consistent with the trend which is seen in the velocity profiles, where the wind side velocity tends to be under-predicted by computation. For $\alpha = 2.9^\circ$, lee side, the absolute agreement between computation and experiment again decreases with increasing x/d , varying from 2% to 27%. Further downstream, the computation overpredicts the measured values for all nosetips.

The absolute comparison of skin friction at $\alpha = 0^\circ$ shows surprisingly good agreement considering the sources of uncertainty in both the computation and experiment. The absolute comparison at $\alpha = 2.9^\circ$ shows that three-dimensional effects are important in the prediction of skin friction. Overall, the relative comparison of skin friction for a blunted configuration to that of the pointed configuration is better than the absolute comparison.

The observed transition behavior may be responsible for some of the disagreement between computation and experiment. The magnitude of uncertainty affecting the skin friction computation in three dimensions approaches the magnitude of the effect of nose bluntness itself. In the future, it may be valuable to compare skin friction for a three-dimensional test case which uses a tripping device, removing the ambiguity associated with transition length and location.

Table 4. Comparison of Skin Friction Coefficient ($C_f \times 10^3$)

$\alpha = 0^\circ$									
	$x/d=3.26$			$x/d=5.05$			$x/d=6.33$		
Nosetip	Comp	Exp	%diff	Comp	Exp	%diff	Comp	Exp	%diff
P	1.44	1.48	- 2.7	1.37	1.36	+ 0.7	1.37	1.41	- 2.8
R1	1.44	1.41	+ 2.1	1.39	1.33	+ 4.5	1.37	1.42	- 3.5
R2	1.34	1.36	- 1.5	1.33	1.32	+ 0.8	1.31	1.34	- 2.2
R3	1.21	1.27	- 4.7	1.20	1.15	+ 4.3	1.20	1.17	- 2.6
F1	N/A	1.42	N/A	N/A	1.34	N/A	N/A	1.33	N/A
F2	N/A	1.26	N/A	N/A	1.19	N/A	N/A	1.21	N/A
F3	1.15	1.22	- 5.7	1.08	1.09	- 0.1	1.09	1.05	+ 3.8

$\alpha = 2.9^\circ$ wind side									
	$x/d=3.26$			$x/d=5.05$			$x/d=6.33$		
Nosetip	Comp	Exp	%diff	Comp	Exp	%diff	Comp	Exp	%diff
P	1.58	1.61	- 1.9	1.53	1.66	- 7.8	1.52	1.66	- 8.4
R1	1.62	1.60	+ 1.3	1.57	1.66	- 5.4	1.52	N/A	N/A
R2	1.62	1.51	+ 7.3	1.50	1.63	- 8.0	1.46	1.69	-13.6
R3	1.55	1.49	+ 4.0	1.40	1.52	- 7.9	1.41	1.56	- 9.6
F1	N/A	1.65	N/A	N/A	1.65	N/A	N/A	1.67	N/A
F2	N/A	1.56	N/A	N/A	1.57	N/A	N/A	1.62	N/A
F3	1.20	1.41	-14.9	1.34	1.39	- 3.6	1.38	1.44	- 4.2

$\alpha = 2.9^\circ$ lee side									
	$x/d=3.26$			$x/d=5.05$			$x/d=6.33$		
Nosetip	Comp	Exp	%diff	Comp	Exp	%diff	Comp	Exp	%diff
P	1.27	1.25	+ 1.6	1.23	1.00	+23.0	1.23	1.00	+23.0
R1	1.29	1.23	+ 4.9	1.23	1.02	+20.6	1.20	0.98	+22.4
R2	1.17	1.13	+ 3.5	1.10	0.81	+25.9	1.05	0.83	+26.5
R3	1.06	1.10	- 3.6	0.97	0.81	+19.8	0.94	0.82	+14.6
F1	N/A	1.23	N/A	N/A	0.93	N/A	N/A	0.92	N/A
F2	N/A	1.04	N/A	N/A	0.80	N/A	N/A	0.79	N/A
F3	0.89	1.03	-13.5	0.91	0.80	+13.8	0.90	0.77	+16.8

VII. SUMMARY

A thin-layer Navier-Stokes computational study has been made to simulate the effects of nosetip bluntness on a body of revolution at Mach 2.95. The objective was to evaluate the accuracy of the computational approach through comparison with experimental data. Two thin-layer Navier-Stokes codes were used in conjunction to compute the flow over the model (excluding the base region). The model consisted of a pointed, spherical, or flat nosetip with up to 25% bluntness, followed by a 3 caliber tangent-ogive and a 5 caliber cylinder. The pointed nosetip provided the reference case for discerning the effects of bluntness. The computational grid for the blunt nosetips was generated using a single-zone, algebraic formulation that wraps the grid around the body to conform with the surface. Boundary layer transition was simulated in the computations based on shadowgraphs which were taken during the experimental study.

For the spherical nosetip case, the comparisons between computation and experiment were mostly within the measurement accuracy for bow shock location and surface pressure distribution. The comparisons of turbulent velocity profiles on the cylinder agreed within about 1% to 5%, except close to the wall. The agreement was substantially better when comparing the profiles relative to the pointed nosetip case. The comparisons of skin friction coefficient on the cylinder varied from 3% to 20%, but the computed values were determined to be sensitive to transition and its modeling. The comparison of skin friction relative to the pointed nosetip case was also better than the absolute agreement. Solutions were obtained on a Cray X-MP/48 using 1 to 3 hours of CPU time and using less than a half million words of memory.

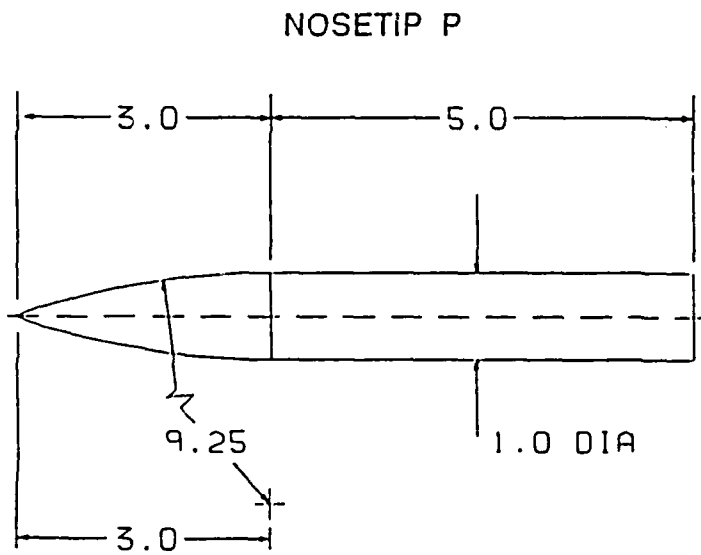
For the flat nosetip case, the comparisons between computation and experiment were mostly within the measurement accuracy for bow shock location, recompression shock location, and surface pressure distribution. The computed surface pressure showed some disagreement close to the corner where a rapid expansion occurs, but still showed strong qualitative agreement. The comparisons of turbulent velocity profiles on the cylinder agreed mostly within 1% to 3%, except close to the wall. The skin friction compared almost as well as the spherical nosetip case. In addition, the computation showed the flow to separate around the corner of the flat nosetip, a flow detail which is difficult, if not impossible, to discern from the shadowgraphs. The flow separation is believed to strongly influence the downstream profiles. The complexity of the flat nosetip flow field is exemplified by the fact that 40 hours of CPU time and 2.5 million words were used on a Cray-2 for the $\alpha = 2.9^\circ$ case. The large amount of computer usage was necessary to obtain an accurate benchmark solution.

The study has demonstrated that the flow details of pointed, spherical, and flat tipped shell can be predicted to a high degree of accuracy. Through comparison with experiment, it has been shown that a single-zone, wrap-around, algebraic grid can be employed to model the laminar flow over a nearly square corner. The computations serve as a benchmark for future CFD efforts in the modeling of supersonic flow over blunted projectiles. The accurate prediction of Magnus characteristics of spinning, flat-tipped shell may now be in hand. One of the remaining challenges is to reduce the computational intensiveness of the problem while ensuring that the accuracy of the flow details is not compromised.

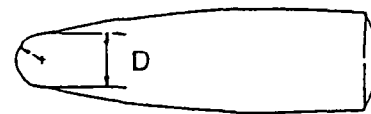
Acknowledgments

The authors gratefully acknowledge the contributions made by the following persons: Dr. Raymond Sedney, for providing ideas and guidance in the comparisons of the nosetip flows, and for reviewing both the interim and final reports; Mr. Lyle D. Kayser, for reviewing the final report; Dr. Walter B. Sturek, for reviewing the evolving manuscript; Dr. James E. Danberg, for providing helpful discussions; and Mr. Glenn A. Smith, Mr. David T. Springer, Mr. Douglas M. Kirby, and Ms. Dorothy J. Spurlin, for helping to organize and present the vast amount of data.

INTENTIONALLY LEFT BLANK.



NOSETIPS R1, R2, R3



NOSETIPS F1, F2, F3



ALL DIMENSIONS IN CALIBERS
(ONE CALIBER = 4.95 cm)

NOSETIP	D
P	0.0
R1, F1	.05
R2, F2	.125
R3, F3	.25

Figure 1. Wind tunnel model and nosetip configurations

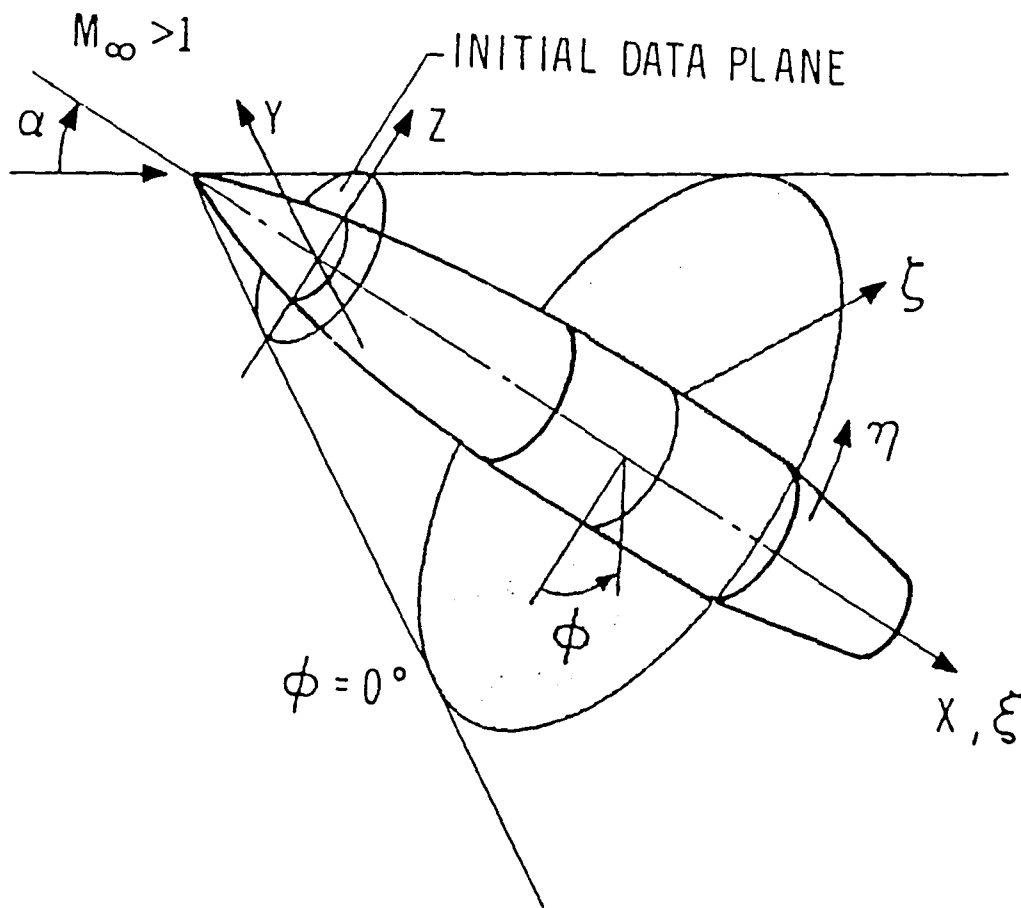


Figure 2. Physical and computational grid coordinates

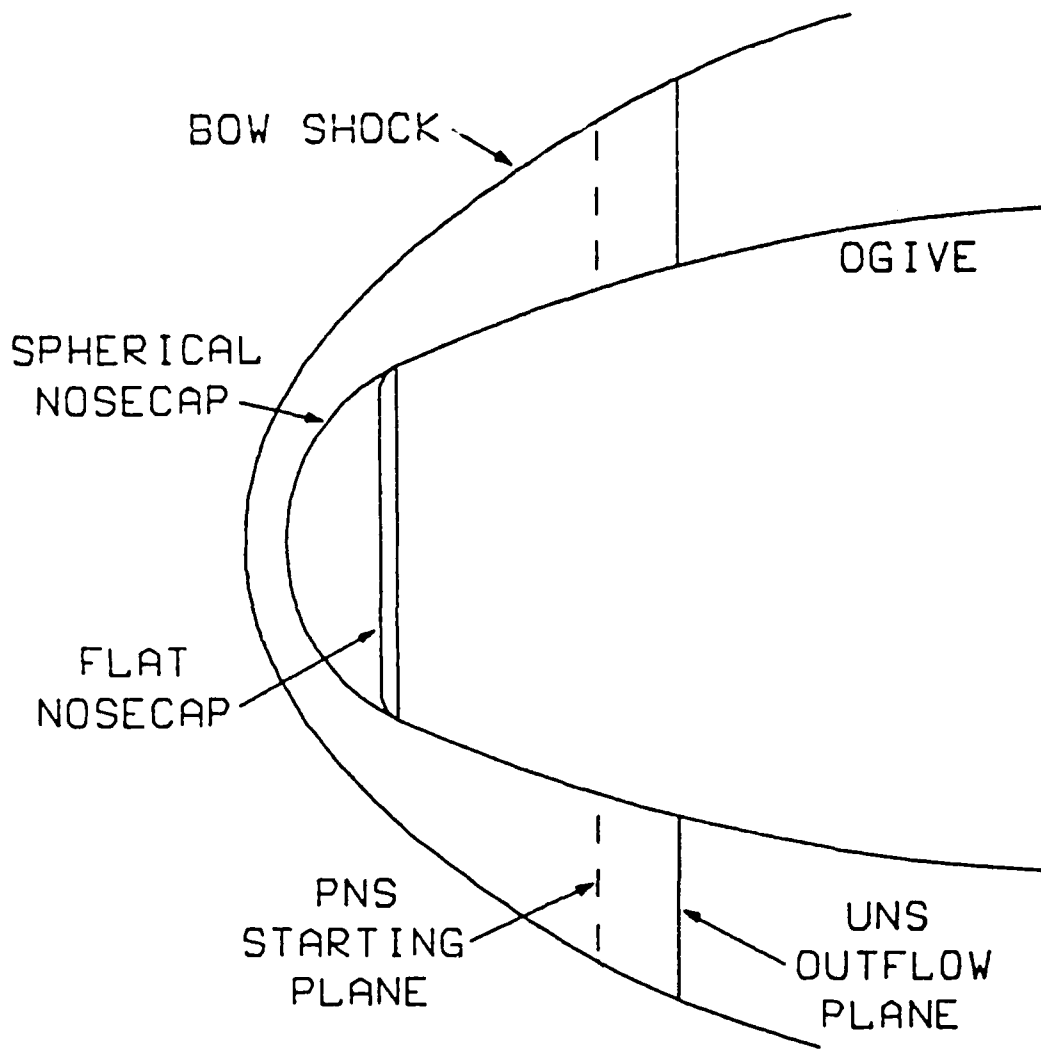


Figure 3. Illustration of code coupling near blunt nosetip

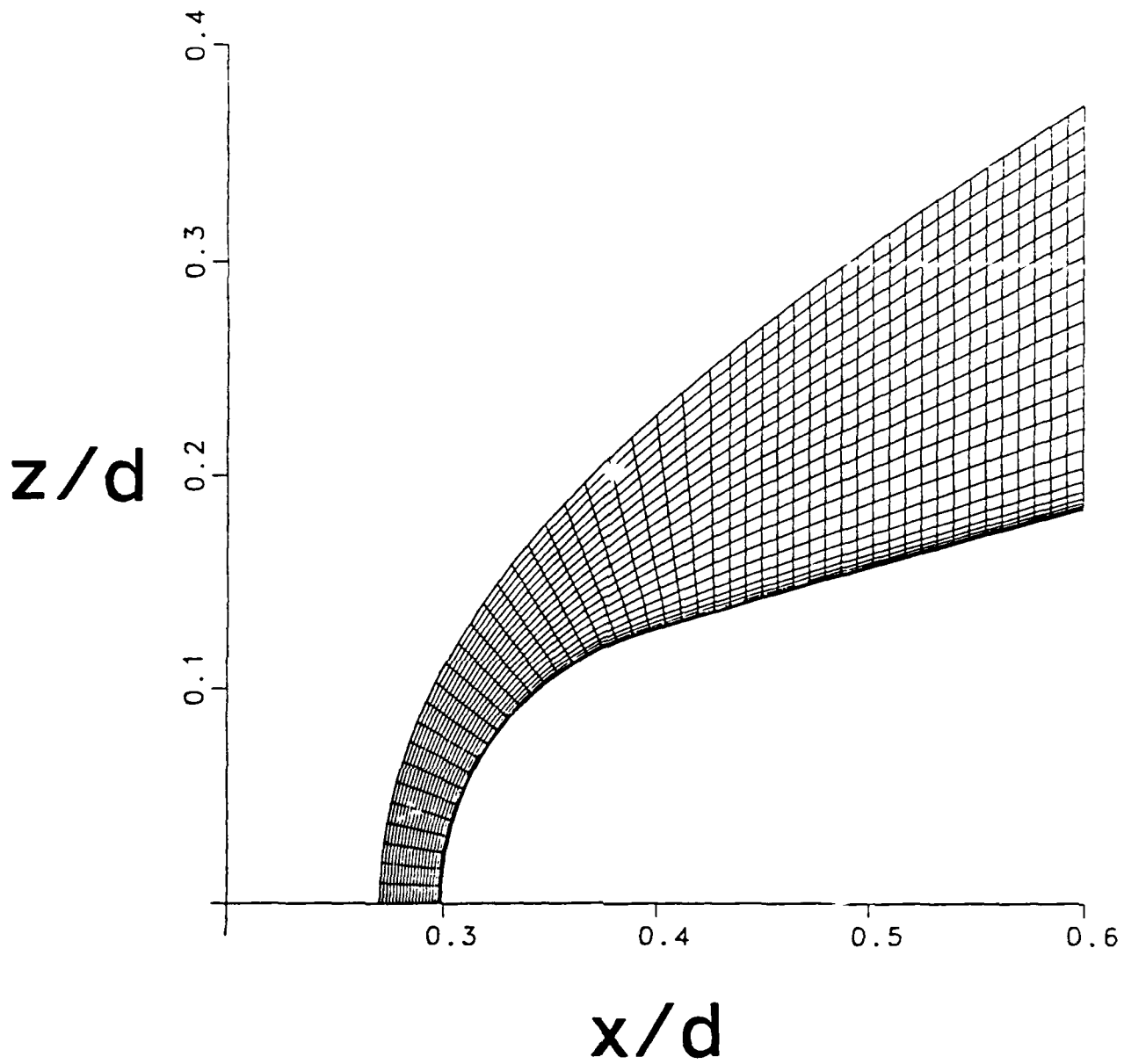


Figure 4. Computational grid for nosetip R3, $\alpha = 0^\circ$

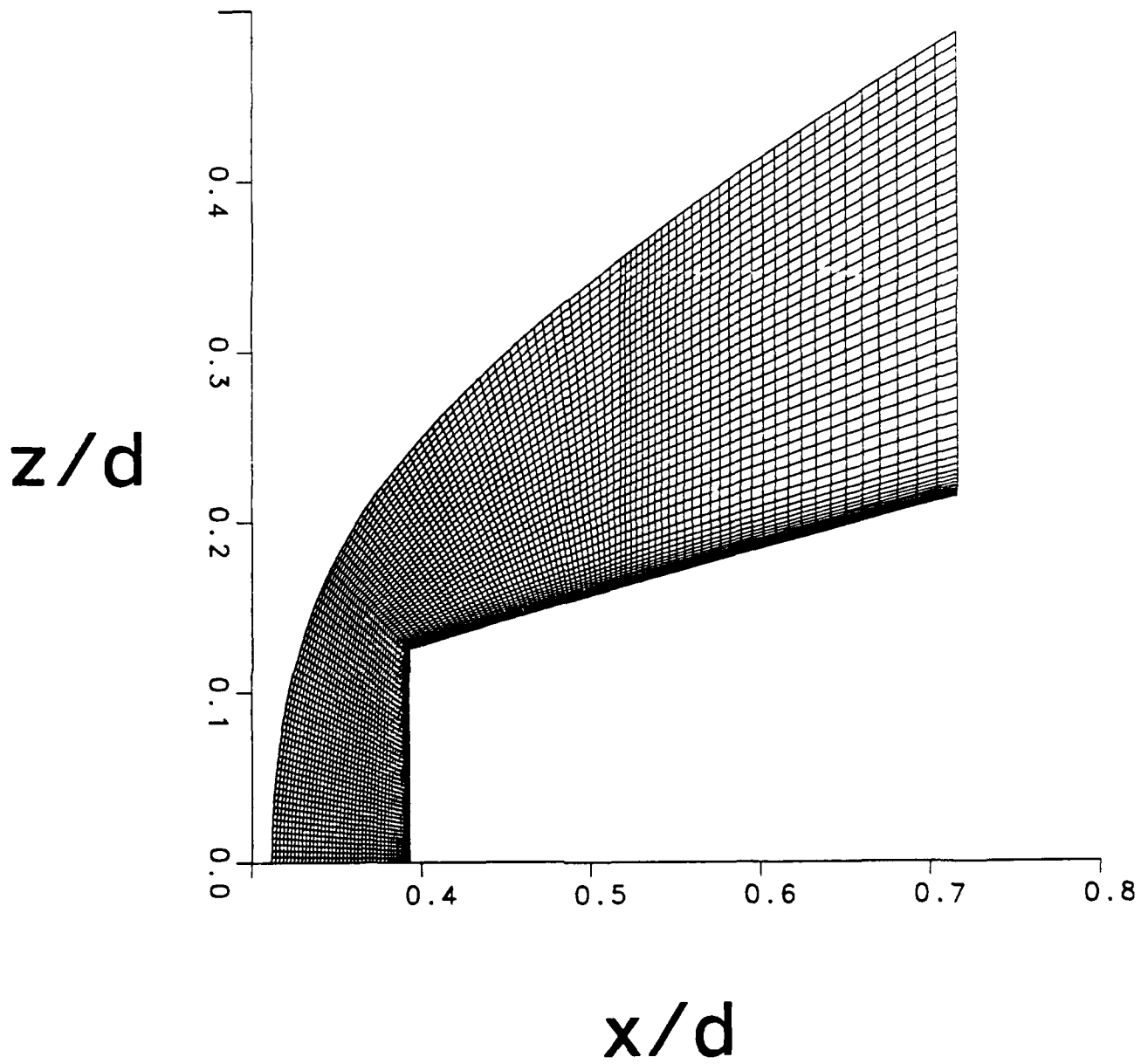


Figure 5. Computational grid for nosetip F3, $\alpha = 0^\circ$

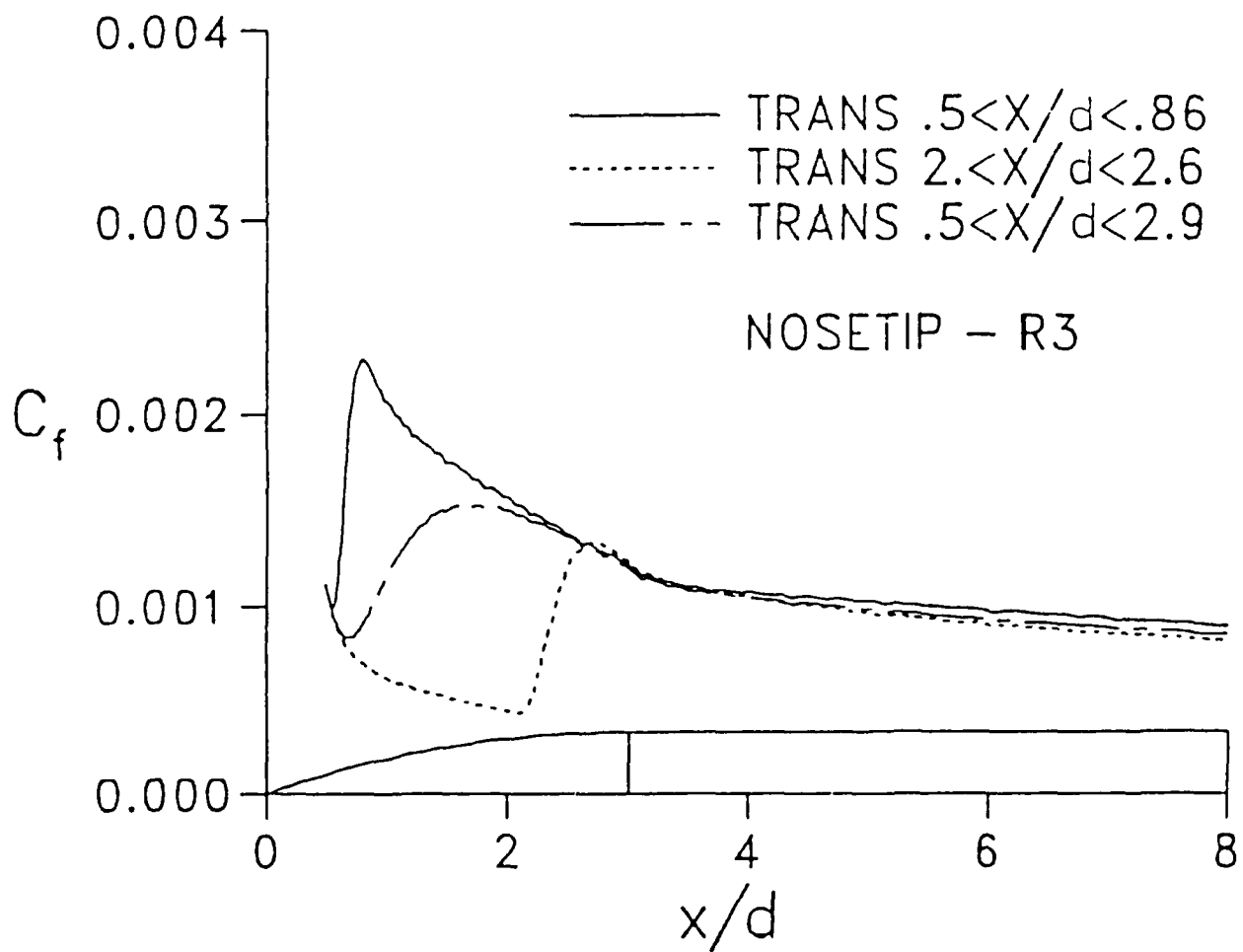


Figure 6. Computed longitudinal skin friction coefficient showing effect of transition model, tip R3, $\alpha = 0^\circ$

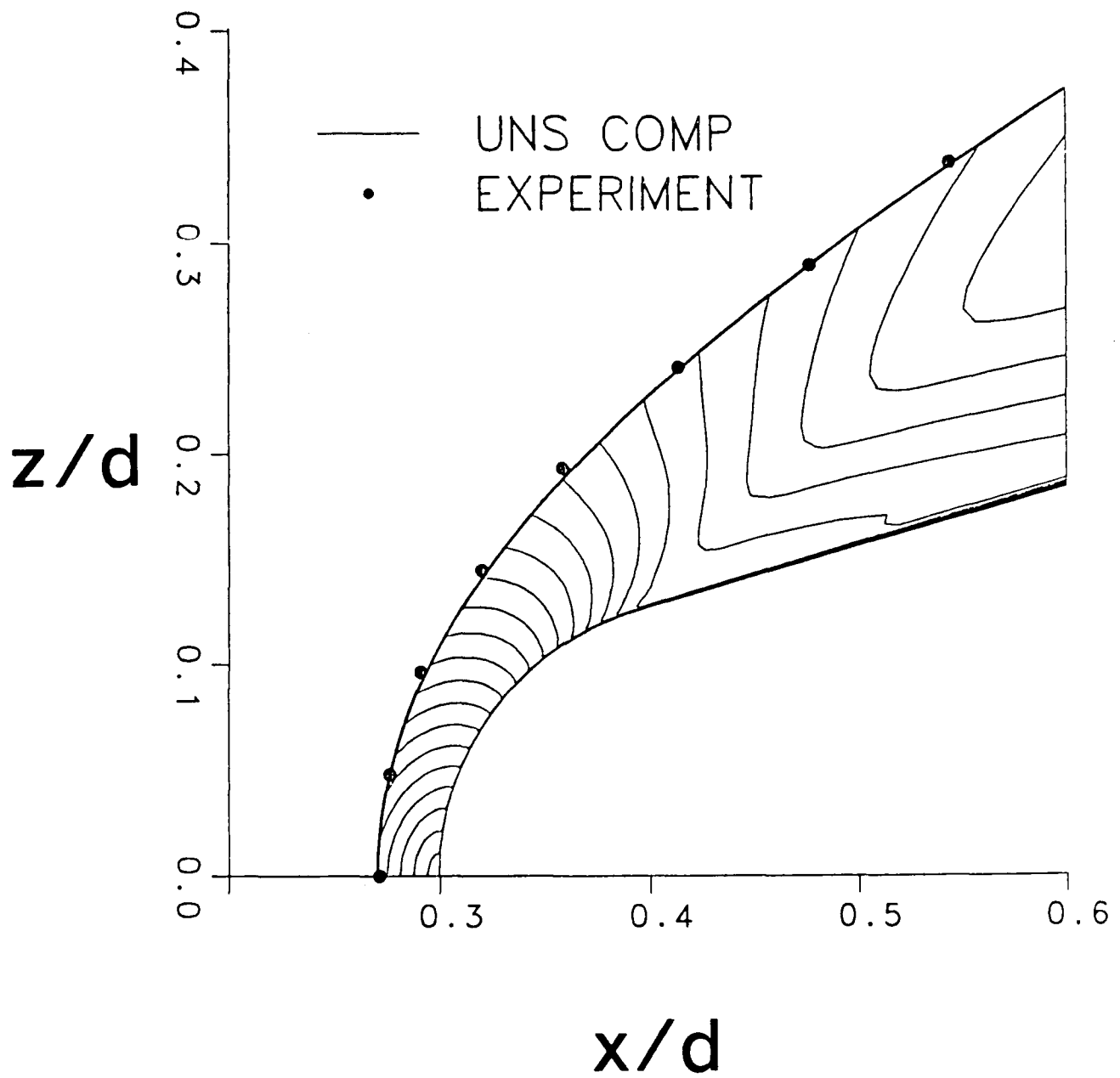


Figure 7. Computed shocks and Mach contours (0.1-2.3 at 0.1 increments) and comparison with measured shocks, tip R3, $\alpha = 0^\circ$

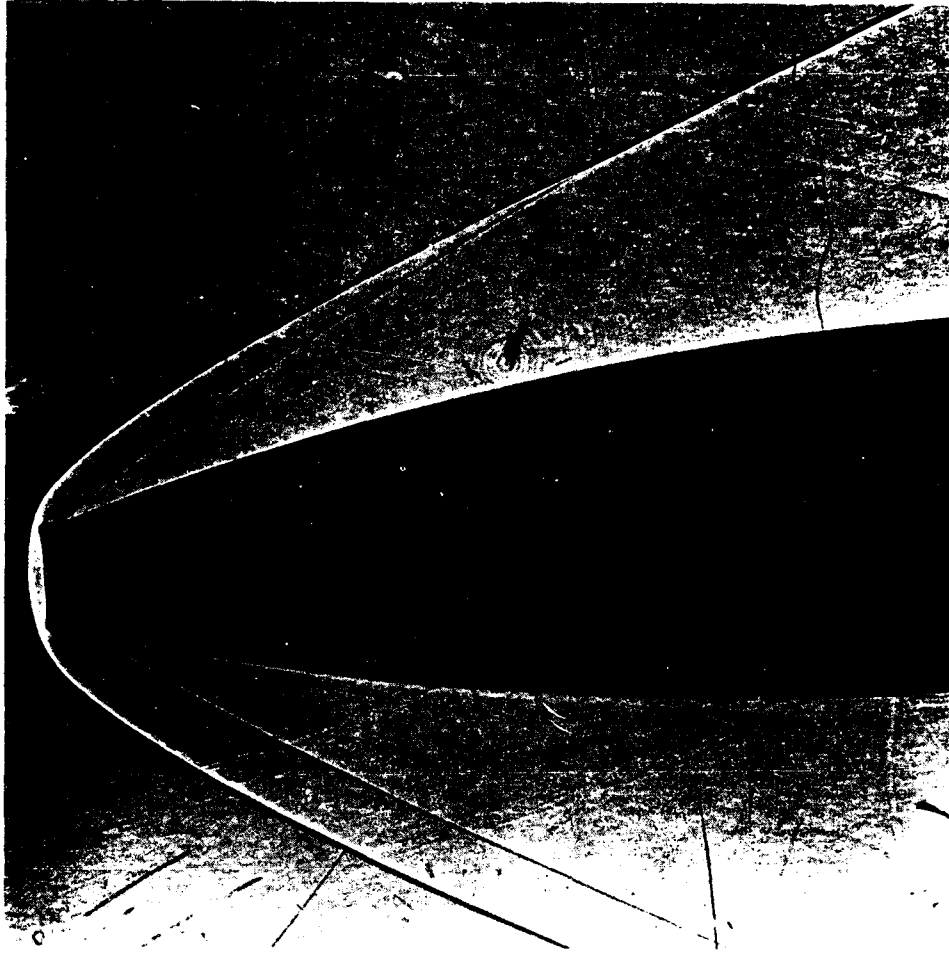


Figure 8. Wind tunnel shadowgraph of flow over nosetip F3, $\alpha = 2.9^\circ$

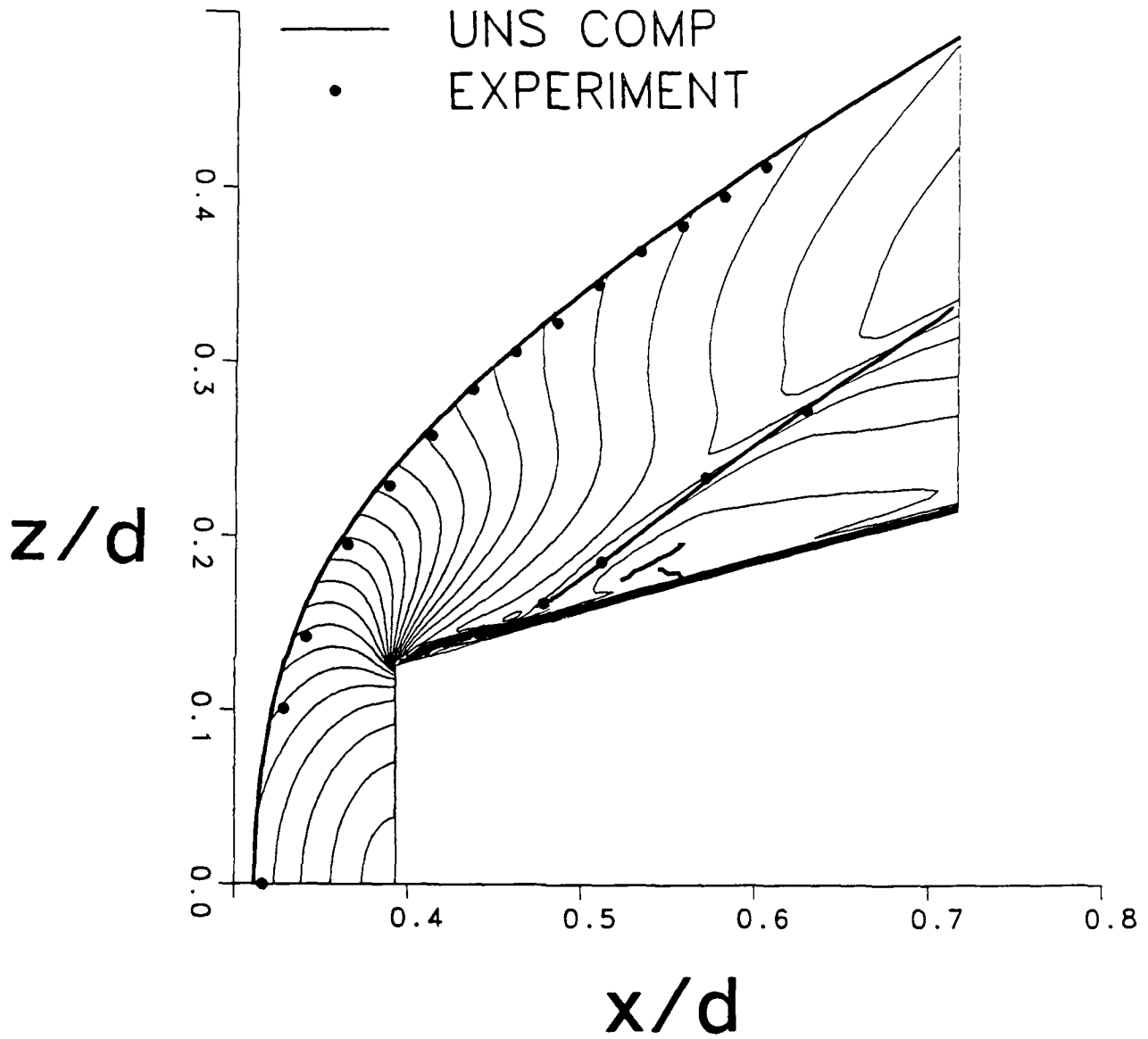


Figure 9. Computed shocks and Mach contours (0.1-2.4 at 0.1 increments) and comparison with measured shocks, tip F3, $\alpha = 0^\circ$

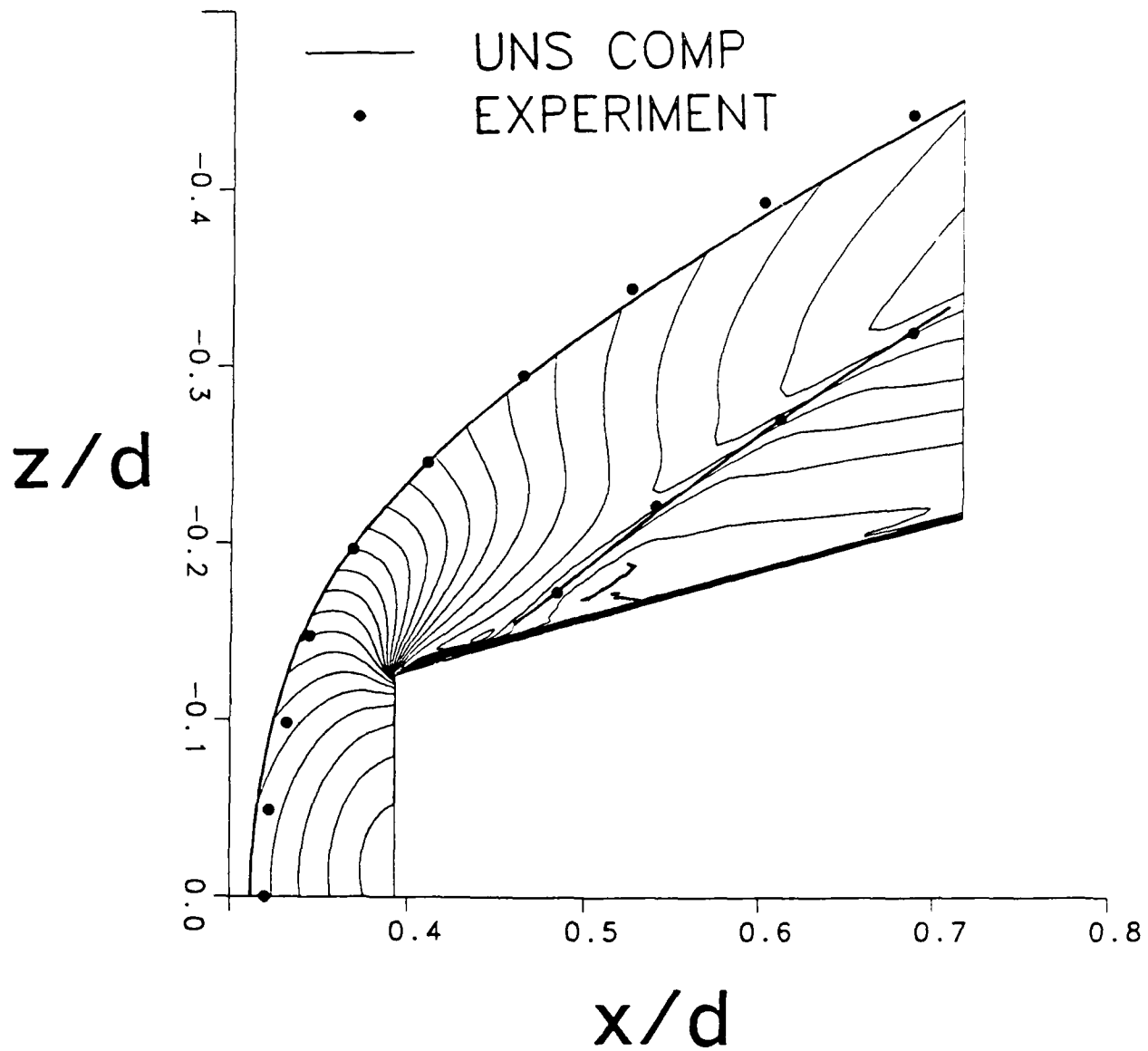


Figure 10. Computed shocks and Mach contours (0.1-2.4 at 0.1 increments) and comparison with measured shocks, tip F3, $\alpha = 2.9^\circ$, wind side

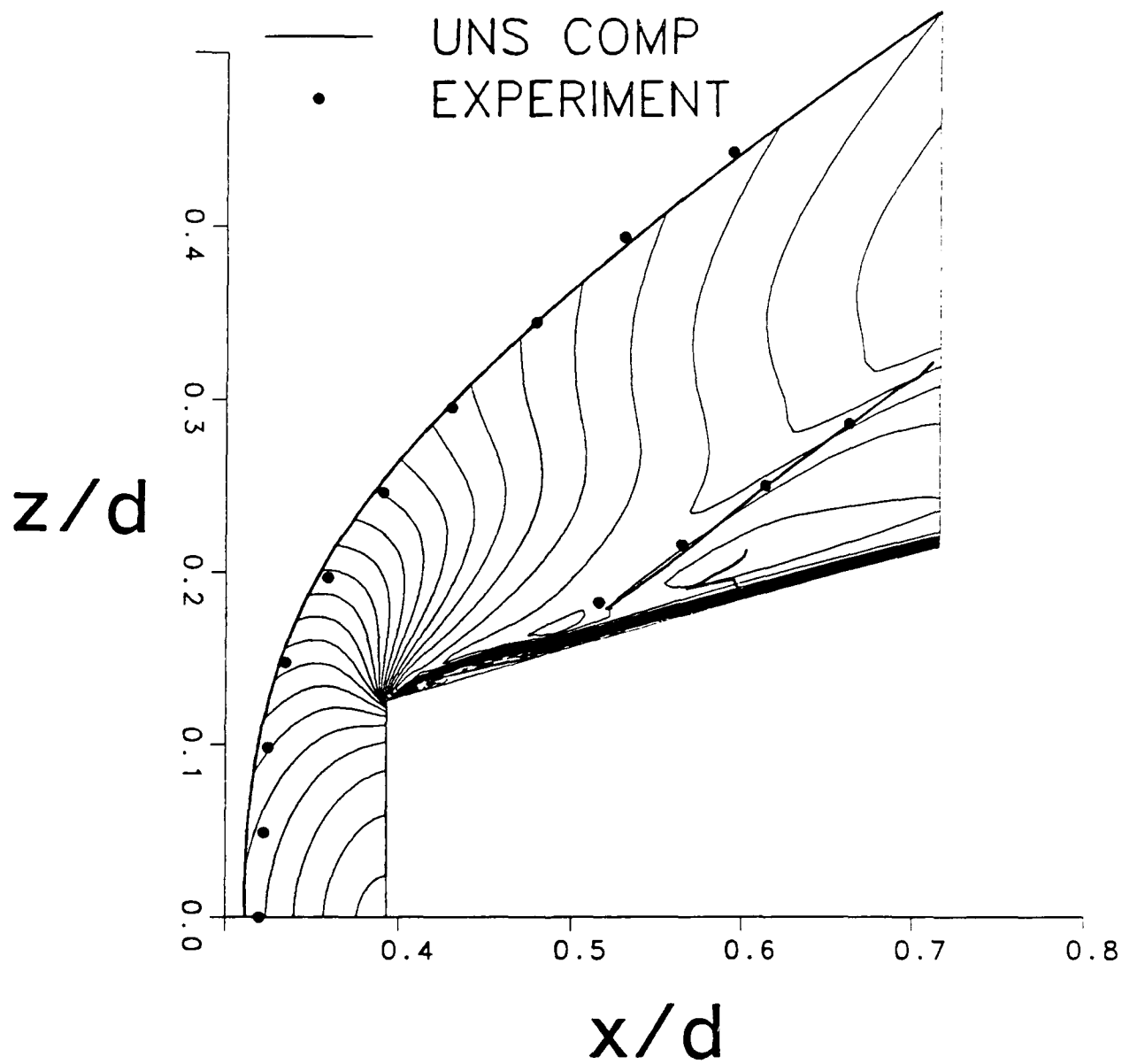


Figure 11. Computed shocks and Mach contours (0.1-2.4 at 0.1 increments) and comparison with measured shocks, tip F3, $\alpha = 2.9^\circ$, lee side

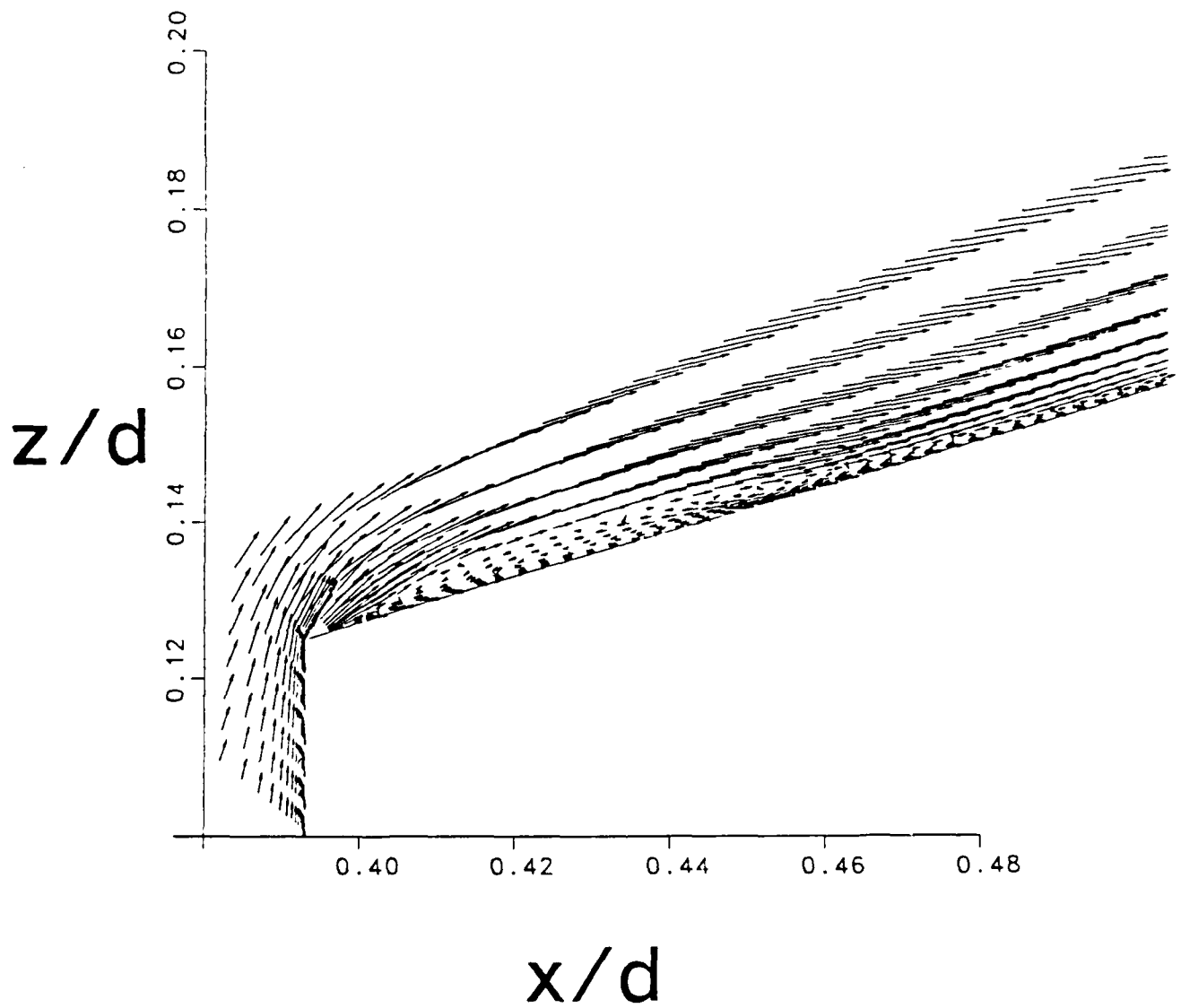


Figure 12. Computed velocity vectors showing flow separation, tip F3, $\alpha = 0^\circ$

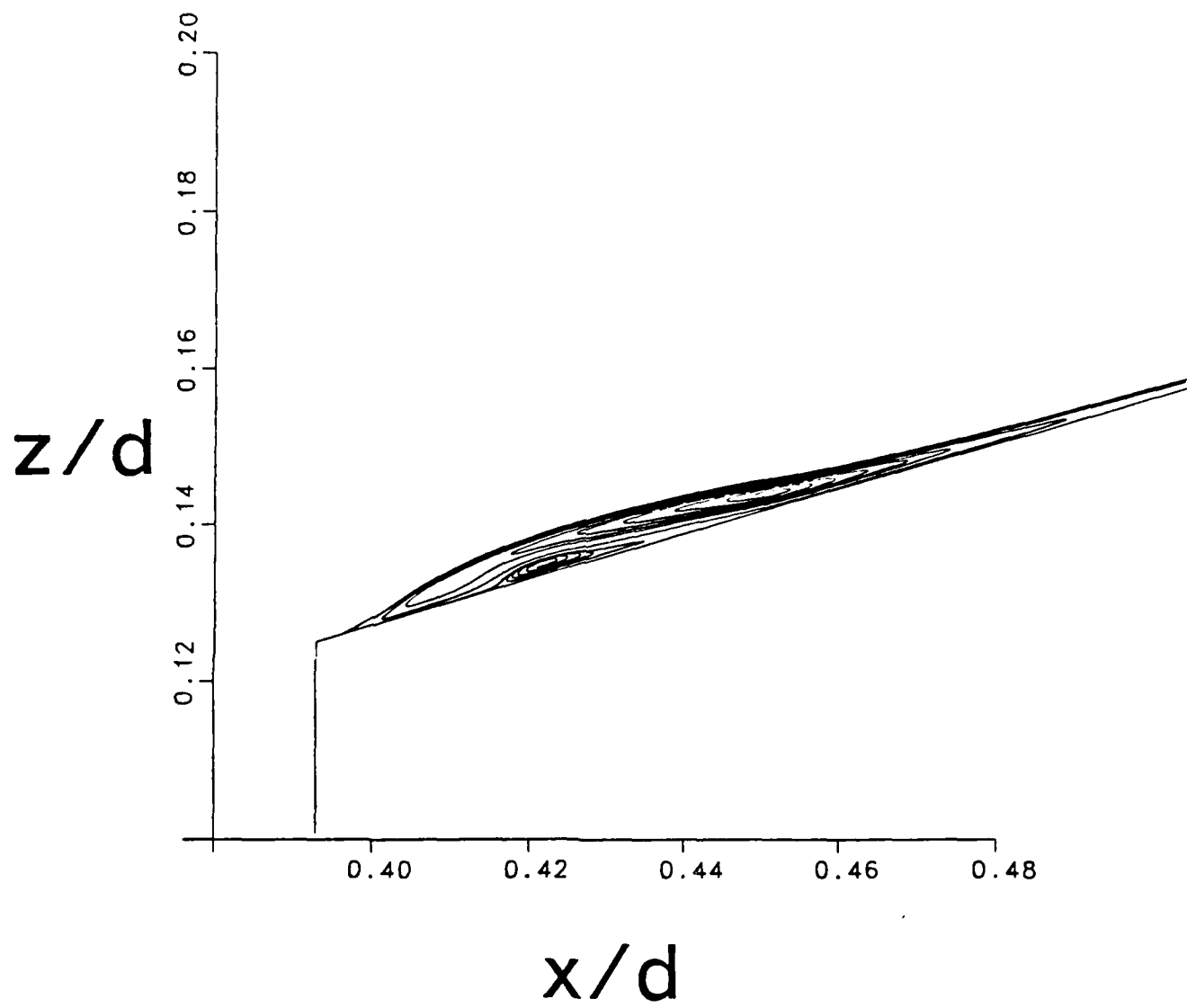


Figure 13. Computed particle paths showing flow separation, tip F3, $\alpha = 0^\circ$

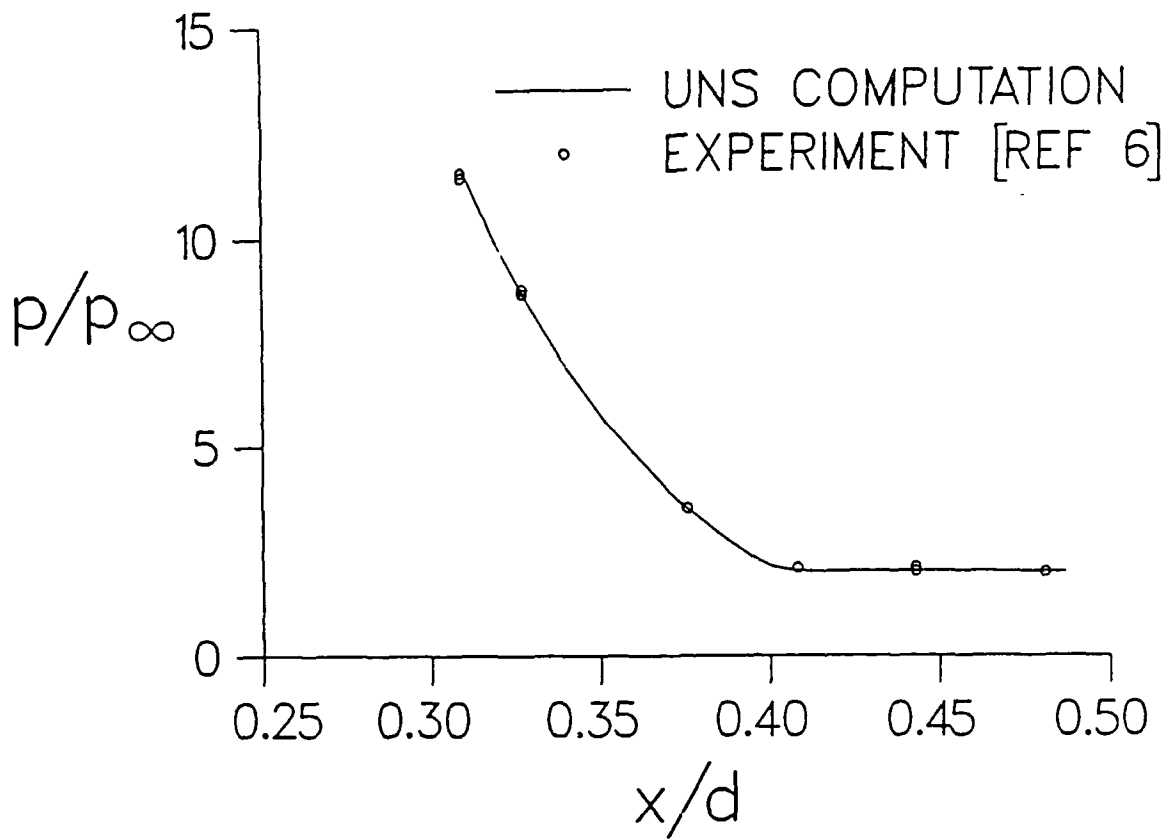


Figure 14. Surface pressure comparison, tip R3, $\alpha = 0^\circ$

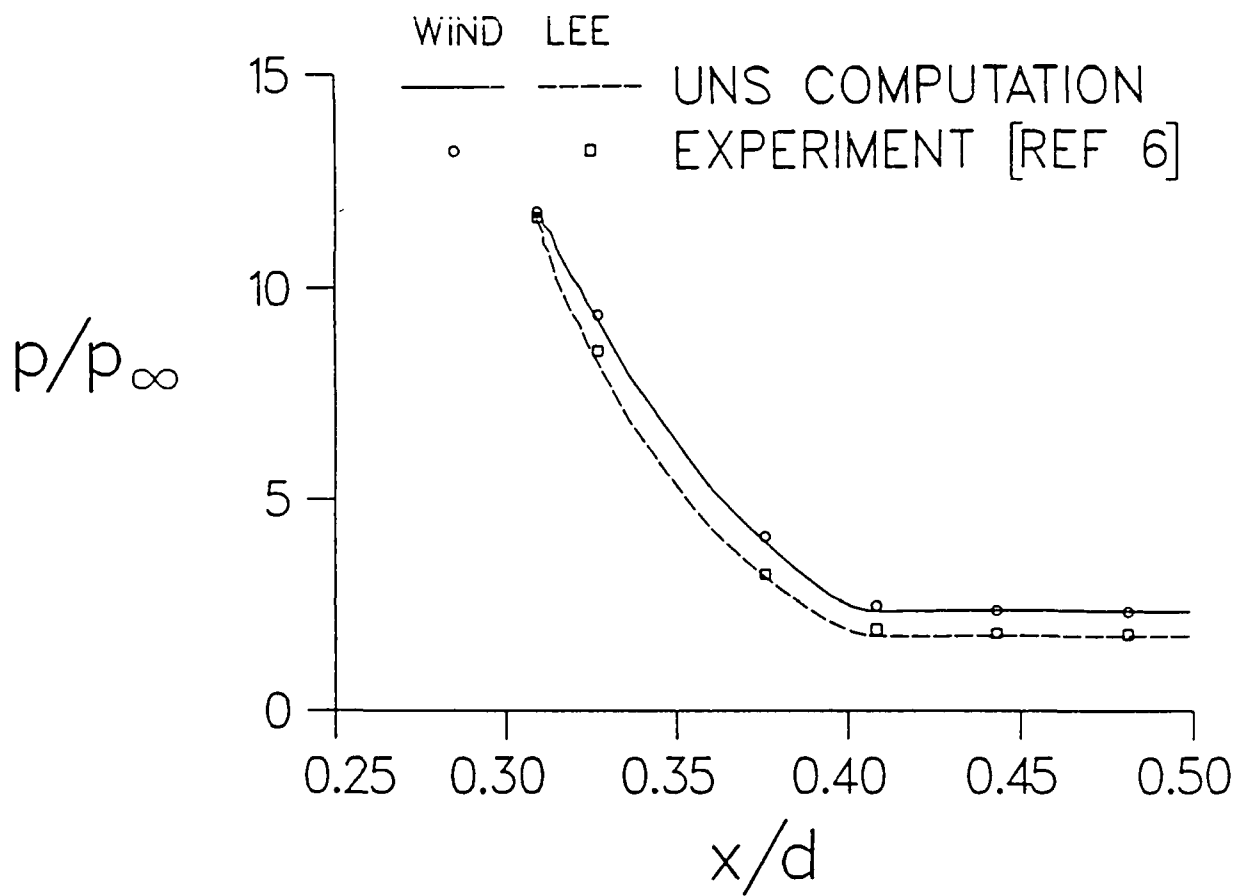


Figure 15. Surface pressure comparison, tip R3, $\alpha = 2.9^\circ$, wind and lee sides

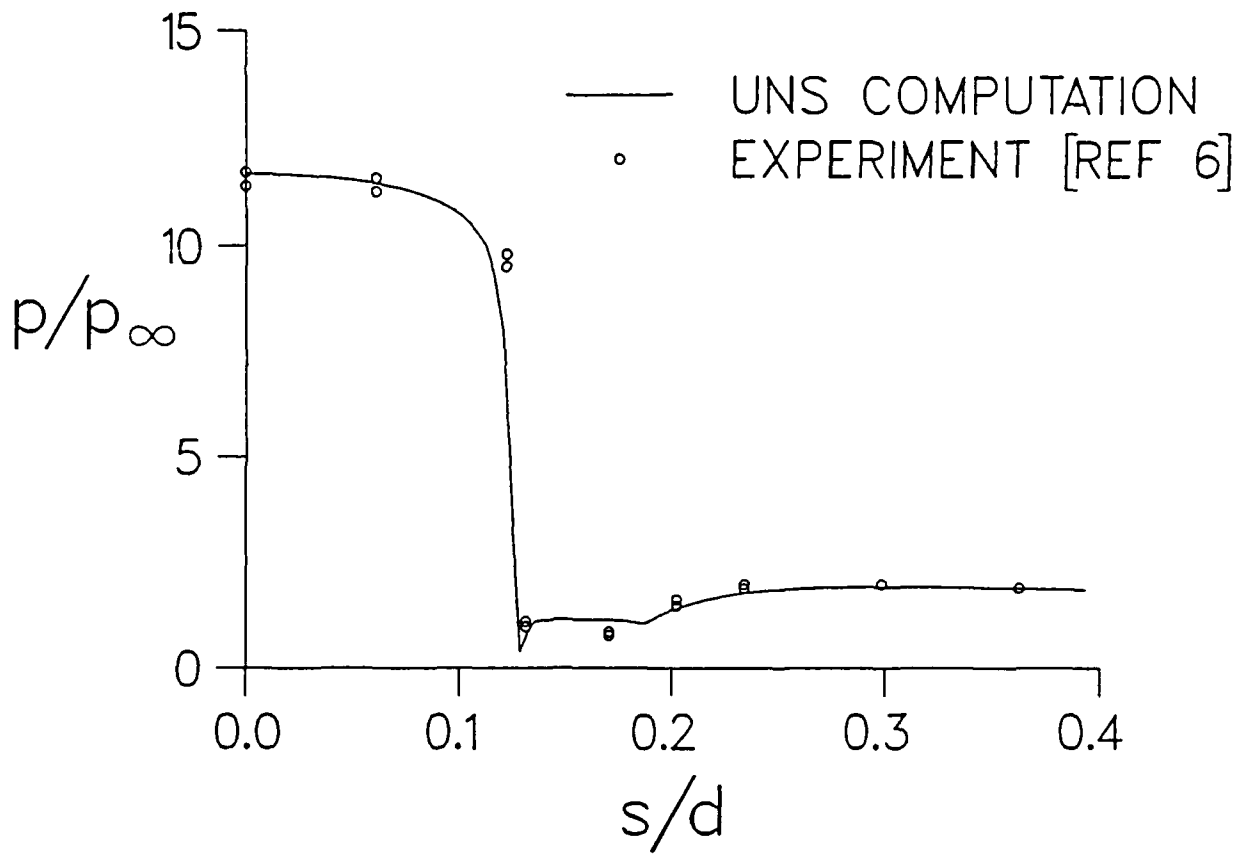


Figure 16. Surface pressure comparison, tip F3, $\alpha = 0^\circ$

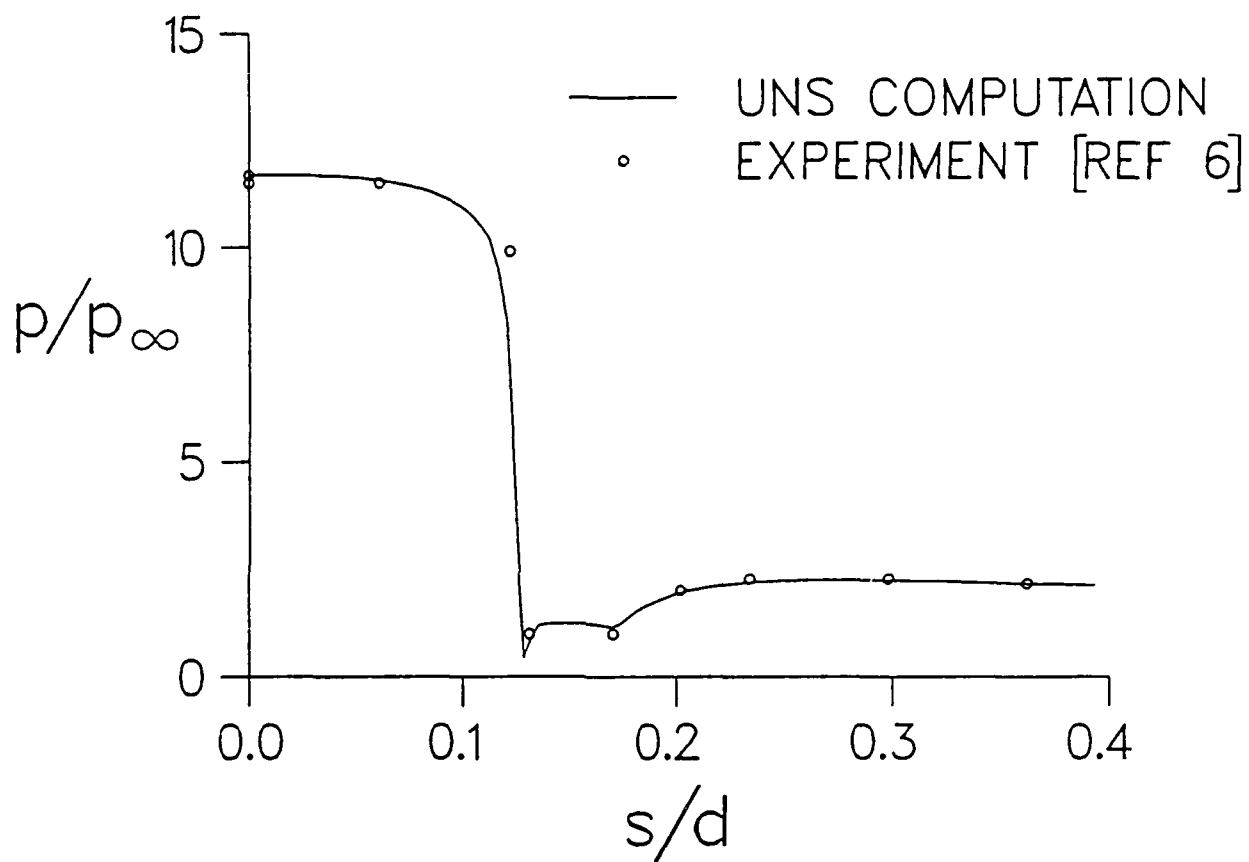


Figure 17. Surface pressure comparison, tip F3, $\alpha = 2.9^\circ$, wind side

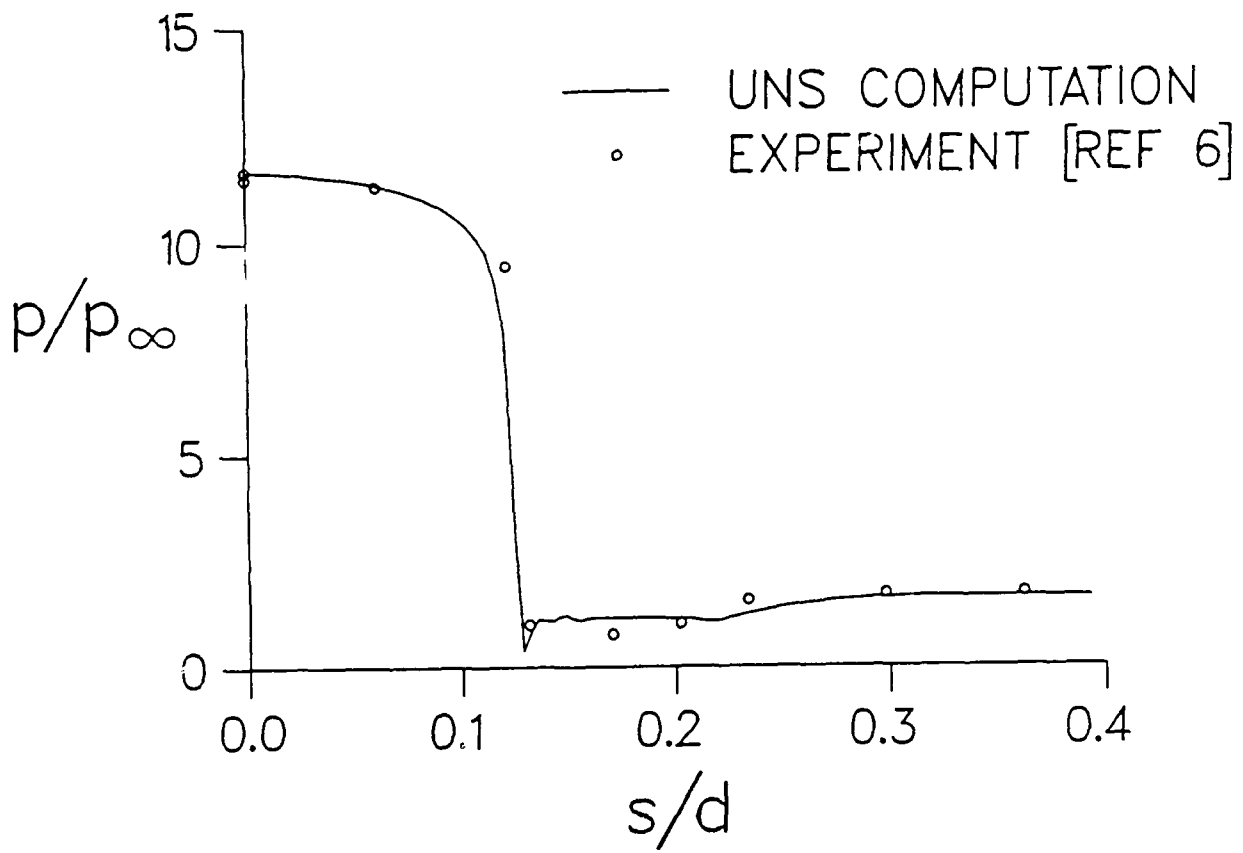


Figure 18. Surface pressure comparison, tip F3, $\alpha = 2.9^\circ$, lee side

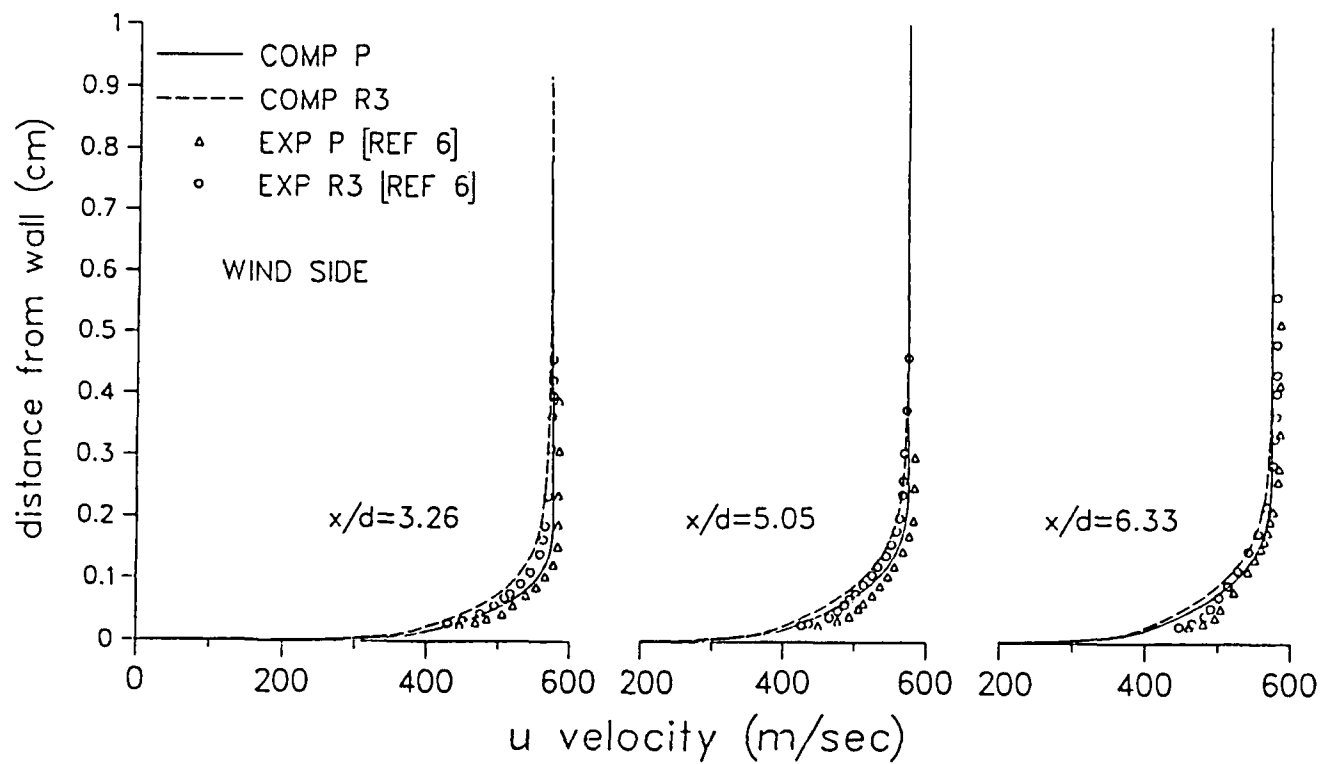


Figure 19. Velocity profile comparisons, tips P and R3, $\alpha = 2.9^\circ$, wind side

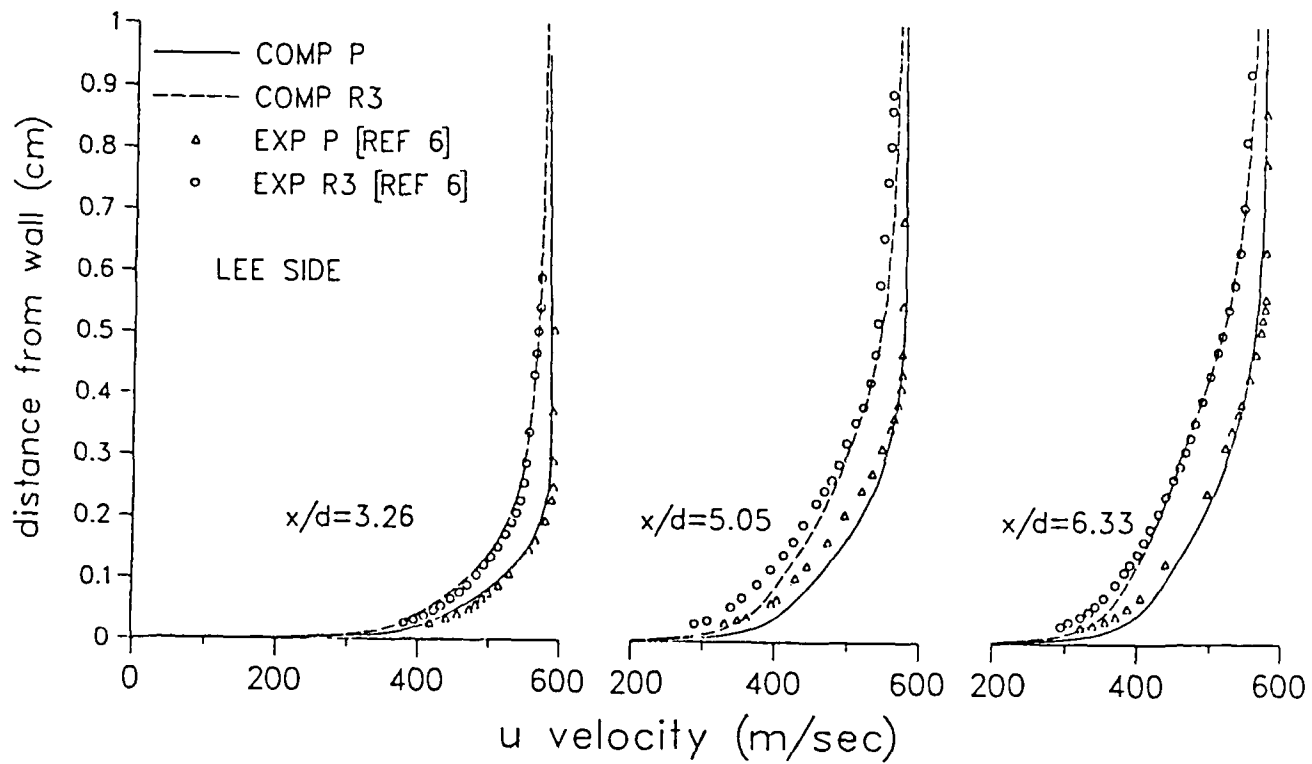


Figure 20. Velocity profile comparisons, tips P and R3, $\alpha = 2.9^\circ$, lee side

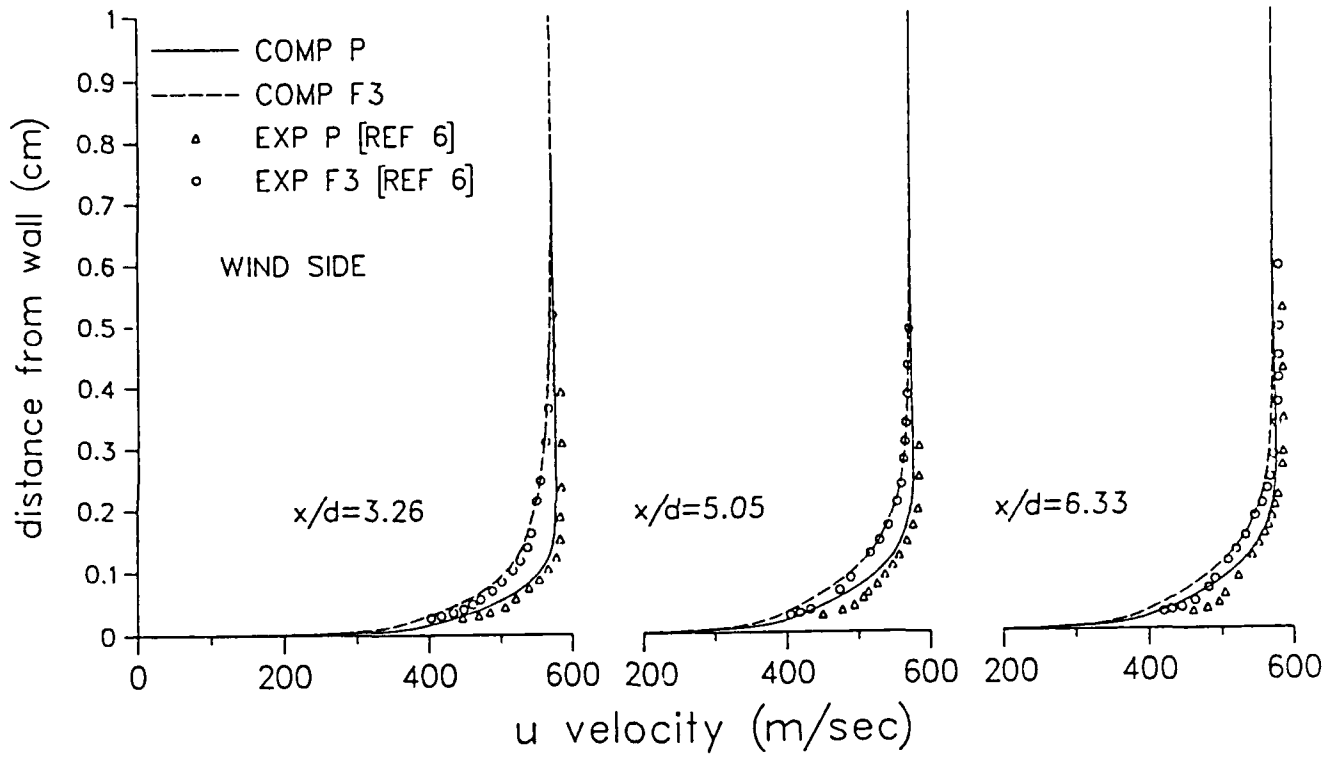


Figure 21. Velocity profile comparisons, tips P and F3, $\alpha = 2.9^\circ$, wind side

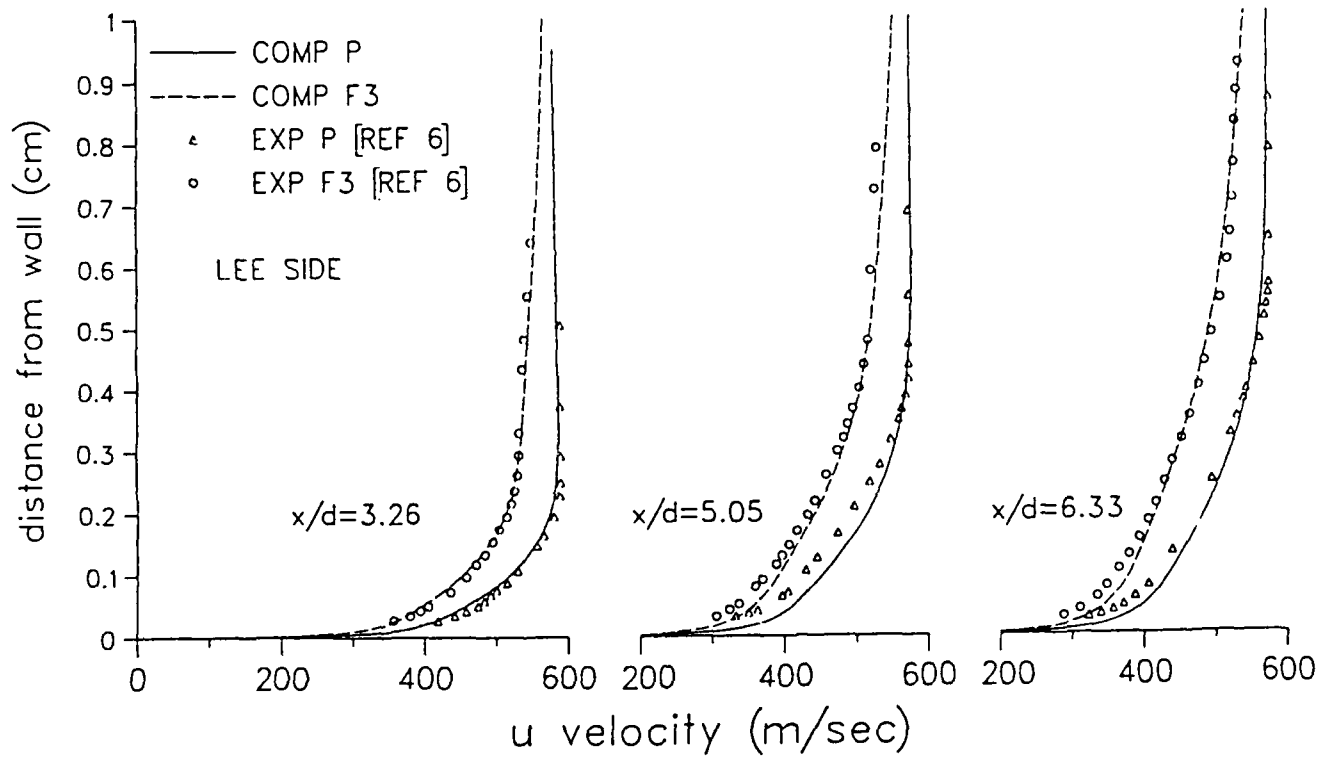


Figure 22. Velocity profile comparisons, tips P and F3, $\alpha = 2.9^\circ$, lee side

References

1. McCoy, R.L., "McDrag'- A Computer Program for Estimating the Drag Coefficients of Projectiles." U.S. Army Ballistic Research Laboratory/ARRADCOM, Aberdeen Proving Ground, MD, ARBRL-TR-02293, February 1981. (AD A09810)
2. Sturek, W.B., Mylin, D.C., Guidos, B.J., and Nietubicz, C.J., "Navier-Stokes Computational Study of the Influence of Shell Geometry on the Magnus Effect at Supersonic Speeds," U.S. Army Ballistic Research Laboratory/ARRADCOM, Aberdeen Proving Ground, MD, ARBRL-TR-02501, June 1983. (AD A130630)
3. Kayser, L.D., "Effects of Small Nose Bluntness on Static Stability and Magnus Characteristics of a Projectile Shape at Mach 0.91 and 3.03," U.S. Army Ballistic Research Laboratory/AMC, Aberdeen Proving Ground, MD, BRL-MR-3535, July 1986. (AD A171734)
4. Dolling, D.S. and Bogdonoff, S.M., "Supersonic, High Reynolds Number Flow over a Tangent Ogive Cylinder at Small Angles of Attack: An Experimental Study and Comparison with Theory," Princeton University Mechanical and Aerospace Engineering Department, Princeton, New Jersey, Report No. 1421-MAE, January 1979.
5. Gray, W.K., Dolling, D.S., and Bogdonoff, S.M., "An Experimental Investigation of Tip Bluntness Effects on the Turbulent Compressible Boundary Layer on an Axisymmetric Body," Princeton University Mechanical and Aerospace Engineering Department, Princeton, New Jersey, Report No. 1530-MAE, May 1981.
6. Dolling, D.S. and Gray, W.K., "Compilation of Wall Pressure and Turbulent Boundary Layer Data for Supersonic, High Reynolds Number Flow over a Blunted Tangent Ogive Cylinder at Small Angles of Attack," Princeton University Mechanical and Aerospace Engineering Department, Princeton, New Jersey, Report No. 1585-MAE, September 1982.
7. Dolling, D.S. and Gray, W.K., "Experimental Study of Supersonic Turbulent Flow on a Blunted Axisymmetric Body," AIAA Journal, Volume 24, No.5, May 1986.
8. Pulliam, T.H. and Steger, J.L., "Implicit Finite-Difference Simulations of Three-Dimensional Compressible Flow," AIAA Journal, Vol. 18, No. 2, February 1980, pp. 159-167.
9. Beam, R. and Warming, R.F., "An Implicit Factored Scheme for the Compressible Navier-Stokes Equations," AIAA Paper No. 78-O257, AIAA 16th Aerospace Sciences Meeting, January 1978.
10. Rizk, Y.M. and Chaussee, D.S., "Three-Dimensional Viscous-Flow Computations using a Directionally Hybrid Implicit-Explicit Procedure," AIAA Paper No. 83-1910, AIAA 16th Fluid and Plasmadynamics Conference, July 1983.
11. Kutler, P., Pedelty, J.A., and Pulliam, T.H. "Supersonic Flow over Three-Dimensional Ablated Nosetips using an Unsteady Implicit Numerical Procedure," AIAA Paper No. 80-0063, AIAA 18th Aerospace Sciences Meeting, January 1980.

12. Rizk, Y.M., Chausee, D.S., and McRae, D.S., "Numerical Simulation of Viscous-Inviscid Interactions on Indented Nose Tips," AIAA Paper No. 82-0290, AIAA 20th Aerospace Sciences Meeting, January 1982.
13. Schiff, L.B. and Steger, J.L., "Numerical Simulation of Steady Supersonic Viscous Flow," AIAA Journal, Vol. 18, No. 12, December 1980, pp. 1421-1430.
14. Rai, M.M. and Chausee, D.S., "New Implicit Boundary Procedures: Theory and Applications," AIAA Paper No. 83-O123, AIAA 21st Aerospace Sciences Meeting, January 1983.
15. Schiff, L.B. and Sturek, W.B., "Numerical Simulation of Steady Supersonic Flow over an Ogive Cylinder Boattail Body," U.S. Army Ballistic Research Laboratory, Aberdeen Proving Ground, Maryland, ARBRL-TR-O2363, September 1981. (AD A106060)
16. Weinacht, P., Guidos, B.J., Kayser, L.D., and Sturek, W.B., "PNS Computations for Spinning and Fin-Stabilized Projectiles at Supersonic Speeds," U.S. Army Ballistic Research Laboratory, Aberdeen Proving Ground, Maryland, ARBRL-MR-3464, September 1985. (AD A160393)
17. Baldwin, B.S. and Lomax, H., "Thin-Layer Approximation and Algebraic Model for Separated Turbulent Flows," AIAA Paper No. 78-0257, AIAA 16th Aerospace Sciences Meeting, January 1978.
18. Dhawan, S. and Narasimha R., "Some Properties of Boundary Layer Flow During the Transition from Laminar to Turbulent Motion," Journal of Fluid Mechanics, Vol. 3, part 4, pp 418-436, 1958.
19. Sedney, R. and Kahl, G.D., "Interferometric Study of the Hypersonic Blunt Body Problem," Ballistic Missiles and Space Technology, Vol. II, pp 337-351, 1961.
20. Giese, J.H. and Bergdolt, V.E., "Interferometric Studies of Supersonic Flows about Truncated Cones," Journal of Applied Physics, Vol.24, No. 11, pp 1339-1396, 1953.
21. Carter, H.S. and Bressette, W.E., "Heat Transfer and Pressure Distribution on Six Blunt Noses at a Mach Number of 2," NACA RM L57C18, April 1957.
22. Buning, P.G., private communication concerning PLOT3D plotting package, Version 3.3, NASA Ames Research Center, Moffett Field, CA, 1987.
23. Liepmann, H.W. and Roshko, A., Elements of Gas Dynamics, Wiley, New York, 1957.
24. Love, E.S., "A Reexamination of the Use of Simple Concepts for Predicting the Shape and Location of Detached Shock Waves," NACA TN 4170, 1957.
25. Kaattari, G.E., "A Method for Predicting Shock Shapes and Pressure Distributions for a Wide Variety of Blunt Bodies at Zero Angle of Attack," NASA TN D-4539, 1968.
26. Guy, T.B., "A Note on the Standoff Distance for Spherical Bodies in Supersonic Flow," AIAA Journal, Vol. 12, No. 3, pp 523-529, March 1974.
27. Van Dyke, M.D., "The Supersonic Blunt-Body Problem - Review and Extension," Journal of the Aeronautical and Space Sciences, pp 458-496, August 1958.

28. Sedney, R., "Shock Wave Curvature for Hypersonic Axisymmetric Flow," Ballistic Research Laboratories, Aberdeen Proving Ground, Maryland, Memorandum Report No. 1093, August 1957. (AD 147438)
29. Weinacht, P., Guidos, B.J., Sturek, W.B., and Hodes, B.A., "PNS Computations for Spinning Shell at Moderate Angles of Attack and for Long L/D Finned Projectiles," U.S. Army Ballistic Research Laboratory, Aberdeen Proving Ground, Maryland, BRL-MR-3522, June 1986. (AD A169531)
30. Sun, C.C., and Childs, M.E., "A Modified Wall-Wake Velocity Profile for Turbulent Compressible Boundary Layers," Journal of Aircraft, Vol. 10, June 1973, pp.381-383.

INTENTIONALLY LEFT BLANK.

List of Symbols

a	speed of sound
B	bow shock bluntness parameter
C_f	skin friction coefficient based on longitudinal shear component and free stream conditions
d	reference diameter of model
D	fuze tip diameter
e	total energy per unit volume of fluid, normalized by $\rho_\infty a_\infty^2$
$\hat{E}, \hat{E}, \hat{F}, \hat{G}$	inviscid flux vectors of transformed gas dynamic equations
M	Mach number
p	pressure normalized by $\rho_\infty a_\infty^2$
p_s	subsonic sublayer pressure
q	vector of dependent variables of gas dynamic equations
\hat{q}	vector of dependent variables of transformed gas dynamic equations
r_s	radial distance between body axis and bow shock
R	bow shock radius at shock vertex
\hat{Re}	Reynolds number, $\rho_\infty a_\infty d / \mu_\infty$
s	distance along body surface from nosetip
\hat{S}	viscous flux vector of transformed gas dynamic equations
t	time
T	temperature
u, v, w	Cartesian velocity components along x, y, z axes, respectively, normalized by a_∞
x_s	axial distance measured from bow shock vertex
x, y, z	physical Cartesian coordinates measured from virtual origin
y^+	distance from wall in boundary layer coordinates

Greek Symbols

α	angle of attack
ξ, η, ζ	transformed coordinates
κ_t	transition intermittency factor
μ	coefficient of viscosity, normalized by free-stream value
μ_l	coefficient of molecular viscosity, normalized by free-stream value
μ_t	coefficient of turbulent viscosity, normalized by free-stream value
ρ	density, normalized by free-stream value
τ	transformed coordinate of time
ϕ	roll angle (circumferential position on the body measured from windward side)

Superscripts

T	transpose of vector
-----	---------------------

Subscripts

w	body surface value
-----	--------------------

∞ free-stream condition
r recovery condition

No of Copies	<u>Organization</u>	No of Copies	<u>Organization</u>
1 (unclass., unlimited)	12 Administrator	1	Commander
1 (unclass., limited)	2 Defense Technical Info Center		US Army Missile Command
1 (classified)	2 ATTN: DTIC-DDA		ATTN: AMSMI-RD-CS-R (DOC)
	Cameron Station		Redstone Arsenal, AL 35898-5010
	Alexandria, VA 22304-6145		
	1 HQDA (SARD-TR)	1	Commander
	WASH DC 20310-0001		US Army Tank Automotive Command
	1 Commander		ATTN: AMSTA-TSL (Technical Library)
	US Army Materiel Command		Warren, MI 48397-5000
	ATTN: AMCDRA-ST	1	Director
	5001 Eisenhower Avenue		US Army TRADOC Analysis Command
	Alexandria, VA 22333-0001		ATTN: ATAA-SL
	1 Commander		White Sands Missile Range, NM 88002-5502
	US Army Laboratory Command	(Class. only) 1	Commandant
	ATTN: AMSLC-DL		US Army Infantry School
	Adelphi, MD 20783-1145		ATTN: ATSH-CD (Security Mgr.)
	2 Commander		Fort Benning, GA 31905-5660
	Armament RD&E Center	(Unclass. only) 1	Commandant
	US Army AMCCOM		US Army Infantry School
	ATTN: SMCAR-MSI		ATTN: ATSH-CD-CSO-OR
	Picatinny Arsenal, NJ 07806-5000		Fort Benning, GA 31905-5660
	2 Commander	(Class. only) 1	The Rand Corporation
	Armament RD&E Center		P.O. Box 2138
	US Army AMCCOM		Santa Monica, CA 90401-2138
	ATTN: SMCAR-TDC		
	Picatinny Arsenal, NJ 07806-5000	1	Air Force Armament Laboratory
	1 Director		ATTN: AFATL/DLODL
	Benet Weapons Laboratory		Eglin AFB, FL 32542-5000
	Armament RD&E Center		<u>Aberdeen Proving Ground</u>
	US Army AMCCOM		Dir, USAMSAA
	ATTN: SMCAR-LCB-TL		ATTN: AMXSY-D
	Watervliet, NY 12189-4050		AMXSY-MP, H. Cohen
	1 Commander		Cdr, USATECOM
	US Army Armament, Munitions		ATTN: AMSTE-TO-F
	and Chemical Command		Cdr, CRDEC, AMCCOM
	ATTN: SMCAR-ESP-L		ATTN: SMCCR-RSP-A
	Rock Island, IL 61299-5000		SMCCR-MU
	1 Commander		SMCCR-MSI
	US Army Aviation Systems Command		Dir, VLAMO
	ATTN: AMSAV-DACL		ATTN: AMSLC-VL-D
	4300 Goodfellow Blvd.		
	St. Louis, MO 63120-1798		
	1 Director		
	US Army Aviation Research		
	and Technology Activity		
	Ames Research Center		
	Moffett Field, CA 94035-1099		

<u>No of Copies</u>	<u>Organization</u>
1	Director National Aeronautics and Space Administration Langley Research Center ATTN: Tech Library Hampton, VA 23365
2	Director Sandia National Laboratories ATTN: Dr. W. Oberkamp Dr. F. Blotner Division 1636 Albuquerque, NM 87185
2	Commander Naval Surface Weapons Center ATTN: Code R44 (Dr. F. Priolo) Code R44 (Dr. A. Wardlaw) White Oak Laboratory Silver Spring, MD 20903-5000
4	Director National Aeronautics and Space Administration Ames Research Center ATTN: M/S N227-8, L. Schiff M/S N258-1, D. Chaussee M/S N258-1, G. Molvik M/S N258-1, Y. Rizk Moffett Field, CA 94035
1	Commander David Taylor Research Center ATTN: J. Gorski Bethesda, MD 20084-5000
1	Princeton University ATTN: Prof. S. Bogdonoff Mechanical and Aerospace Department Princeton, NJ 08544
1	Stanford University Department of Applied Mechanics ATTN: Prof. M. Van Dyke Stanford, CA 94305
1	The University of Texas at Austin ATTN: Prof. D.S. Dolling Department of Aerospace Engineering and Engineering Mechanics Austin, TX 78712-1085
1	University of Delaware ATTN: Prof. L. Schwartz Department of Mechanical Engineering Newark, DE 19713

USER EVALUATION SHEET/CHANGE OF ADDRESS

This Laboratory undertakes a continuing effort to improve the quality of the reports it publishes. Your comments/answers to the items/questions below will aid us in our efforts.

1. BRL Report Number BRL-TR-3076 Date of Report JANUARY 1990
2. Date Report Received _____
3. Does this report satisfy a need? (Comment on purpose, related project, or other area of interest for which the report will be used.) _____

4. How specifically, is the report being used? (Information source, design data, procedure, source of ideas, etc.) _____

5. Has the information in this report led to any quantitative savings as far as man-hours or dollars saved, operating costs avoided or efficiencies achieved, etc? If so, please elaborate. _____

6. General Comments. What do you think should be changed to improve future reports? (Indicate changes to organization, technical content, format, etc.) _____

CURRENT ADDRESS

Name _____

Organization _____

Address _____

City, State, Zip _____

7. If indicating a Change of Address or Address Correction, please provide the New or Correct Address in Block 6 above and the Old or Incorrect address below.

OLD ADDRESS

Name _____

Organization _____

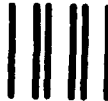
Address _____

City, State, Zip _____

(Remove this sheet, fold as indicated, staple or tape closed, and mail.)

FOLD HERE

Director
U.S. Army Ballistic Research Laboratory
ATTN: SLCBR-DD-T
Aberdeen Proving Ground, MD 21005-5066



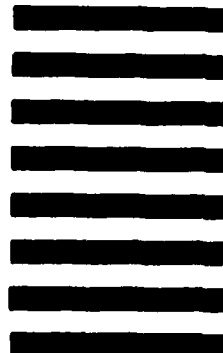
NO POSTAGE
NECESSARY
IF MAILED
IN THE
UNITED STATES

OFFICIAL BUSINESS

BUSINESS REPLY MAIL
FIRST CLASS PERMIT NO 12062 WASHINGTON, DC

POSTAGE WILL BE PAID BY DEPARTMENT OF THE ARMY

Director
U.S. Army Ballistic Research Laboratory
ATTN: SLCBR-DD-T
Aberdeen Proving Ground, MD 21005-9989



FOLD HERE